The Pretornadic Phase of the Goshen County, Wyoming, Supercell of 5 June 2009 Intercepted by VORTEX2. Part II: Intensification of Low-Level Rotation

PAUL MARKOWSKI, YVETTE RICHARDSON, AND JAMES MARQUIS

Department of Meteorology, The Pennsylvania State University, University Park, Pennsylvania

ROBERT DAVIES-JONES*

NOAA/National Severe Storms Laboratory, Norman, Oklahoma

JOSHUA WURMAN, KAREN KOSIBA, AND PAUL ROBINSON

Center for Severe Weather Research, Boulder, Colorado

ERIK RASMUSSEN

Rasmussen Systems, Mesa, Colorado

DAVID DOWELL

NOAA/Earth System Research Laboratory, Boulder, Colorado

ABSTRACT

The dynamical processes responsible for the intensification of low-level rotation prior to tornadogenesis are investigated in the Goshen County, Wyoming, supercell of 5 June 2009 intercepted by the second Verification of the Origins of Rotation in Tornadoes Experiment (VORTEX2). The circulation of material circuits that converge upon the low-level mesocyclone is principally acquired along the southern periphery of the forward-flank precipitation region, which is a corridor characterized by a horizontal buoyancy gradient; thus, much of the circulation appears to have been baroclinically generated. The descending reflectivity core (DRC) documented in Part I of this paper has an important modulating influence on the circulation of the material circuits. A circuit that converges upon the low-level mesocyclone center prior to the DRC's arrival at low levels (approximately the arrival of the 55-dBZ reflectivity isosurface in this case) loses some of its previously acquired circulation during the final few minutes of its approach. In contrast, a circuit that approaches the low-level mesocyclone center after the DRC arrives at low levels does not experience the same adversity.

An analysis of the evolution of angular momentum within a circular control disk centered on the low-level mesocyclone reveals that the area-averaged angular momentum in the nearby surroundings of the low-level mesocyclone increases while the mesocyclone is occluding and warm-sector air is being displaced from the near surroundings. The occlusion process reduces the overall negative vertical flux of angular momentum into the control disk and enables the area-averaged angular momentum to continue increasing even though the positive radial influx of angular momentum is decreasing in time.

---

* Emeritus.

Corresponding author address: Dr. Paul Markowski, Department of Meteorology, The Pennsylvania State University, 503 Walker Building, University Park, PA 16802.
E-mail: pmarkowski@psu.edu

1. Introduction

One focus of our ongoing research is the relative role of environmental vorticity versus storm-generated vorticity in tornadogenesis and maintenance. In supercell environments, which are characterized by relatively large vertical shear of the horizontal wind, the horizontal

vorticity is typically on the order of 10^{-2} s^{-1} in the lower troposphere. In contrast, vorticity can be generated internally within a storm by horizontal buoyancy gradients (i.e., baroclinity). The generation of vorticity by baroclinity is principally horizontal and easily can produce vorticity having the same order of magnitude as the ambient horizontal vorticity in a supercell environment. The largest horizontal buoyancy gradients typically are found on the edges of clouds and precipitation regions. Both environmental and storm-generated vorticity can be tilted and stretched in any direction by wind velocity gradients.

It is well known that both environmental and storm-generated vorticity are important in the development of mesocyclones and tornadoes within supercells (Rotunno and Klemp 1985, hereafter RK85). Mesocyclones that develop at *midlevels* in a supercell updraft arise from the tilting of environmental vorticity (Rotunno 1981; Lilly 1982; Davies-Jones 1984). On the other hand, the development of rotation *next to the ground* occurs near the interface of downdraft and updraft because horizontal vorticity tilted by an updraft alone acquires a vertical component only as it rises away from the surface[1] (Davies-Jones 1982a,b). Air passing through the left side of a downdraft can acquire cyclonic vorticity through two mechanisms. The first is the tilting of environmental crosswise vorticity (positive speed shear) within the downdraft [see top panel of Fig. 9 in Davies-Jones and Brooks (1993, hereafter DJB93)]. The second is baroclinic generation of streamwise horizontal vorticity and subsequent tilting (DJB93; Davies-Jones 2000; Davies-Jones et al. 2001). If the environmental vorticity is streamwise and baroclinic vorticity generation is absent or neglected, the vorticity vector of a parcel will be tilted downward during its descent, but will be horizontal again when the parcel exits the downdraft (see middle panel of DJB93's Fig. 9). Vertical vorticity can arise along the descending part of the trajectory if there is baroclinic production (see bottom panel of DJB93's Fig. 9). This second mechanism has been found to be important in the development of near-ground rotation in the supercell simulations of DJB93, Adlerman et al. (1999), and RK85 (although this aspect of their Fig. 8 was not discussed, the figure reveals the growth of cyclonic vorticity during the descent of a trajectory along which the upstream vorticity was highly streamwise).

Although observations, simulations, and theory all point to the importance of both environmental and storm-generated vorticity, what is less obvious is how their relative importance might vary from storm to storm and perhaps determine the likelihood of tornadogenesis. For example, temperature observations obtained by mobile mesonets have found that tornado formation is unlikely in supercells having outflow associated with rear-flank and forward-flank downdrafts (RFD and FFD, respectively) that is very cold relative to the inflow (e.g., temperature deficits >5 K), at least at the surface (Markowski et al. 2002; Shabbott and Markowski 2006; Grzych et al. 2007; Hirth et al. 2008). These observations of negatively buoyant outflow being unfavorable for tornadogenesis suggest that, although baroclinic vorticity generation is crucial along descending trajectories, excessive negative buoyancy that might accompany particularly large baroclinic vorticity generation could be unfavorable, assuming that the magnitude of the horizontal buoyancy gradients, on average, increases with increasing negative buoyancy. It also seems plausible that the orientation of the environmental vorticity would determine to what extent the environmental vorticity contributes to the development of low-level rotation.

Markowski et al. (2012, hereafter Part I) documented the pretornadic phase of the Goshen County, Wyoming, tornadic supercell intercepted on 5 June 2009 by the second Verification of the Origins of Rotation in Tornadoes Experiment (VORTEX2; Wurman et al. 2012). The evolution of the vortex lines (e.g., the development of arching vortex lines that join the counterrotating vortices straddling the hook echo; e.g., see Fig. 20 in Part I) was similar to what has been seen before and, as also has been argued before, was suggestive of significant baroclinic vorticity generation (Straka et al. 2007; Markowski et al. 2008, 2011; Marquis et al. 2012). One goal of this article is to investigate the origins of low-level rotation more quantitatively. We are also interested in the abrupt intensification of low-level rotation in the 2142–2148 UTC period (the vortex reached tornado strength at 2152 UTC; Kosiba et al. 2012, manuscript submitted to *Mon. Wea. Rev.*), which was preceded by the development of a descending reflectivity core (DRC; Rasmussen et al. 2006; Kennedy et al. 2007a,b; Byko et al. 2009). Considerable interest has surrounded DRCs recently, given that they have been found to contribute to the formation or evolution of hook echoes, and occasionally have been observed to precede the rapid development or intensification of low-level rotation, as was the case in the Goshen County storm. In the Goshen County storm, a DRC developed at midlevels at 2139 UTC (Fig. 12 of Part I). The DRC subsequently

---

[1] Vertical vorticity can be produced close to the ground if vortex lines near the surface are turned abruptly upward by intense gradients of upward velocity, but this is highly improbable without a strong vortex being present already at low levels (Adlerman et al. 1999, p. 2045).

descended to the surface and was associated with a rapid increase in the vertical vorticity and circulation of the low-level mesocyclone (Figs. 15 and 20 of Part I).

The purpose of this paper is (i) to quantify the relative contributions to the rotation of the pretornadic low-level mesocyclone of the Goshen County storm from environmental vorticity and storm-generated vorticity, and (ii) to investigate the dynamical role of the precipitation associated with the DRC, which was closely linked to the rapid increase in rotation after 2142 UTC. Sections 2 and 3 describe our motivation and methodology, respectively. Section 4 examines the evolution of circulation about material circuits that are tracked backward from the mesocyclone region. The analyses quantify the bulk contribution of baroclinic vorticity generation to the circulation of the low-level mesocyclone and shed some light on the role of the DRC. Section 5 complements section 4 by examining the evolution of angular momentum within a fixed area centered on the circulation. Sections 6 and 7 discuss and summarize the findings.

2. Motivation for a Lagrangian circulation analysis

Although there naturally is great interest in the development of vertical vorticity along trajectories that pass through the circulation center or location of maximum vertical vorticity (ζ_{max}), the analysis of the vorticity vector and its forcings along these trajectories is hampered by (i) the tendency for these trajectories to drop below the lowest level of dual-Doppler scanning ($z = 0.25$ km in the Goshen County storm during the pretornadic phase)[2] or be "captured" by the low-level circulation,[3] (ii) errors in the calculation of the terms in the vorticity equation (numerous finite differences are involved) and their interpolation to trajectories, and (iii) trajectory errors (even perfect three-dimensional wind retrievals do not guarantee error-free trajectories, given that our wind syntheses have relatively coarse time

resolution compared with the speed at which flows can evolve, especially near ζ_{max}). With respect to (i) and (ii), it is virtually impossible to avoid downward extrapolation entirely when computing trajectories near the low-level circulation, but we are more comfortable downward-extrapolating horizontal wind components to trajectories than downward-extrapolating velocity derivatives. The amount of downward extrapolation along backward trajectories can be reduced by specifying trajectory origins outside of the region of strong low-level convergence/ascent that often accompanies ζ_{max}. Concerning (iii), trajectory errors also can be mitigated by avoiding the large accelerations and rapid evolution of the wind field often observed in the immediate vicinity of ζ_{max}.

Because of the aforementioned difficulties in analyzing vorticity changes along trajectories near the location of ζ_{max}, we favor an analysis of the circulation about material circuits traced backward in time from the low-level mesocyclone region. We follow the approach of RK85 and DJB93, who investigated the development of low-level circulation in simulated supercells. The material circuit approach provides indirect information about the bulk contribution to the mesocyclone's circulation from baroclinic vorticity generation. Moreover, circulation calculations are less sensitive to random errors in the wind synthesis than the calculation of terms in the vorticity equation, because the calculations involve integrals of the velocity components rather than derivatives.

From Bjerknes' theorem, the change in circulation following a material circuit is, to the inviscid Boussinesq approximation,

$$\frac{DC}{Dt} = \oint B \, dz, \qquad (1)$$

where $C = \oint \mathbf{v} \cdot \mathbf{dl}$ is the circulation, $\mathbf{v} = u\mathbf{i} + v\mathbf{j} + w\mathbf{k}$ is the wind velocity, $\mathbf{dl}$ is an element of the circuit along which the integration is performed (in a counterclockwise direction), B is the buoyancy, and the effect of the Coriolis acceleration has been neglected. The circulation around a circuit is equal to the surface integral of vorticity (i.e., the vorticity flux). Equivalently, the circulation per unit area is equal to the average normal vorticity within the area.

A small material circuit surrounding the vorticity maximum cannot be traced backward accurately in time because of the large spatial and temporal gradients in velocity near the maximum. Therefore a larger circuit was chosen despite the fact that the average vorticity in the enclosed area is less. It is assumed that the origins of rotation in the immediate surroundings of the vorticity maximum are relevant for how the vorticity maximum itself forms and evolves (note that the rapid increase

---

[2] This unfortunate reality can be inferred from Part I's Fig. 16, which shows forward trajectories originating within and around the low-level vorticity maximum. It is evident that most trajectories originating within roughly a kilometer of the circulation center, even as high as a few kilometers above the surface, would quickly drop below the data horizon if integrated backward.

[3] By "captured" we are referring to backward trajectories near ζ_{max} that sometimes (unrealistically) cannot escape the vortex when integrated backward (e.g., Kosiba et al. 2012, manuscript submitted to *Mon. Wea. Rev.*). The issue probably stems from the radar scans inadequately resolving or overshooting the low-level horizontal convergence. The depth of the horizontal convergence at the base of a vortex interacting with the surface thins as the vortex intensifies.

in maximum vertical vorticity from 2142 to 2148 UTC evident in Fig. 7 of Part I was accompanied by a rapid increase in larger-scale circulation). However, large low-level circulation is clearly not a sufficient condition for tornadogenesis, as evidenced by the fact that even nontornadic low-level mesocyclones can have large circulation (e.g., Fig. 19 of Part I).

The analysis of circulation about a material circuit performed by RK85 showed that the baroclinically generated horizontal vorticity was the dominant contributor to the circulation of the low-level mesocyclone in their simulated storm. The analysis of circulation about a material circuit only has been done a few times since RK85's study, and almost exclusively for simulated storms. DJB93, Walko (1993), Trapp and Fiedler (1995),[4] Mashiko et al. (2009),[5] and Nowotarski et al. (2011)[6] also have analyzed circulation about material circuits in supercell simulations, and Markowski et al. (2011) performed an analysis for three nontornadic low-level mesocyclones, although the backward integration period was limited by the data to 5 min. *We still cannot say more than 25 years after RK85's circulation analysis whether circulation evolves similarly in observed storms, whether there are any fundamental differences in the evolution of circulation between nontornadic and tornadic storms, or even how the magnitude of the circulation that develops about the circuits depends on the strength of the cold pool and characteristics of the environmental hodograph.* We believe circulation analysis is an attractive approach for observational studies like this one that target the role of baroclinic vorticity generation, given the challenges in directly observing the buoyancy fields of storms and the aforementioned pitfalls of derivative and trajectory calculations in close proximity to ζ_{max}.

3. Methodology

The three-dimensional wind fields used in this study are from the "fine" grids described in section 2a of Part I

(also refer to Table 1 in Part I). Wind syntheses are available at 2-min intervals from 2142 to 2148 UTC. A Barnes smoothing parameter of $\kappa_0 = 0.48$ km^2 was used on the first pass of the two-pass objective analysis used to interpolate edited radial velocity data to the grid. On the second pass, the smoothing parameter was reduced by 70%. The grid spacing is 0.25 km, and the grid moves with the mean velocity of the low-level circulation in order to reduce interpolation errors in the Lagrangian calculations (the low-level circulation is centered near the origin).

No extrapolation was permitted in the gridding of the raw radar data. To apply the lower boundary condition (the vertical velocity must vanish at $z = 0$) during the three-dimensional wind synthesis, the coefficients in the dual-Doppler equations that involve direction cosines and radial velocities [e.g., Ray et al. 1980, their Eq. (5)] were extrapolated to $z = 0$ from the lowest overlying grid level with data (the lowest level with data is $z = 0.25$ km). For all of the analyses in Part I, extrapolated winds were reset to "missing" after each wind synthesis was completed. However, some portions of the material circuits inevitably drop below the data horizon when traced backward in time despite our best attempts to avoid this.

We allow horizontal winds from $z = 0.25$ km to be extrapolated to the lowest grid level (nominally $z = 0$ km, though this height probably should be regarded as the anemometer level) assuming a log wind profile via

$$\mathbf{v}_1 = \left[-|\mathbf{v}_2| \frac{\ln(z_a/z_0)}{\ln(z_2/z_0)} \sin\psi, \ -|\mathbf{v}_2| \frac{\ln(z_a/z_0)}{\ln(z_2/z_0)} \cos\psi \right], \quad (2)$$

where $\mathbf{v}_1$ is the horizontal velocity at the lowest grid level, z_a is the anemometer level assumed to represent the height of the lowest grid level, $\mathbf{v}_2$ is the horizontal velocity at the second grid level at height z_2 ($=0.25$ km), z_0 is the roughness length, and ψ is the wind direction ($0°$ is from the north, $90°$ is from the east, etc.).[7] The horizontal velocities must be converted to ground-relative winds (the wind synthesis was performed on a translating grid) prior to extrapolating. The above approach assumes a neutrally stratified surface layer and that the wind at $z = 0.25$ km is in or not far above the surface layer. Although a neutral stratification is generally not a good assumption in outflow or sunshine, the correction

[4] The numerical studies of Walko (1993) and Trapp and Fiedler (1995) investigated the processes that generate rotation at the surface using heat sources and sinks in a dry model, rather than simulating actual supercells.

[5] Mashiko et al. (2009) simulated a supercell within the outer rainbands of a landfalling tropical cyclone. This simulation is probably not the best to compare to the Goshen County storm because the environment of the simulated supercell possessed considerable background vertical vorticity. Moreover, the material circuits were only tracked backward for 2 min. In that short period, the circulation was relatively constant (see their Fig. 20).

[6] Nowotarski et al. (2011) investigated the generation of circulation in supercells that were initiated above a stable boundary layer.

[7] The log wind profile for a neutrally stratified surface layer is $|\mathbf{v}| = (u_*/k) \ln(z/z_0)$, where u_* is the friction velocity and k is von Kármán's constant. In (2), the fraction u_*/k is determined from the wind speed at $z = 0.25$ km and an assumed roughness length [i.e., $u_*/k = |\mathbf{v}_2|/\ln(z_2/z_0)$].

for a statically stable or unstable surface layer is small in strong near-surface winds and wind shear. Material circuit analyses were performed with z_0 ranging from 1 to 5 cm (appropriate for southeastern Wyoming) and z_a ranging from 3 to 10 m AGL. Analyses also were conducted by setting the horizontal velocity at the lowest grid level equal to the horizontal velocity at $z = 0.25$ km (this is the approach taken in most past dual-Doppler analyses). It is our hope that the suite of analyses brackets the range of plausible circulation trends.

Material circuits were projected backward in time using a fourth-order Runge–Kutta algorithm. A time step of 15 s was used, and the three-dimensional wind fields were assumed to vary linearly in time between dual-Doppler analyses. The spatial interpolation was trilinear. To extend trajectories farther back in time, we assumed a steady state in the 2132–2142 UTC period. Although we would have preferred not to rely on this assumption, the alternative would have been Lagrangian analyses terminating only a short distance upstream of the mesocyclone. It is unlikely that a Lagrangian analysis of such short duration (2–6 min for the material circuits analyzed in section 4) would be of much use. Our hope is that the region traversed by the circuits prior to 2142 UTC—the forward flank outflow and environmental air to the east of the updraft—is sufficiently steady for the accompanying analyses to have at least qualitative credibility (we would expect these regions to be much steadier than the low-level mesocyclone region). Synthetic data tests presented in the appendix suggest that the steadiness assumption was not a major source of errors in the trajectory and circulation calculations presented in section 4.

4. Lagrangian circulation analysis of the pretornadic Goshen County low-level mesocyclone

The evolution of circulation is investigated for a pair of material circuits integrated backward in time from the low-level mesocyclone region. One circuit, hereafter *circuit A*, encircles the mesocyclone at $z = 0.75$ km at 2148 UTC, by which time both low-level vertical vorticity and circulation have grown very large in magnitude and tornadogenesis is only 4 min away (Fig. 9 of Part I). The other circuit, *circuit B*, encircles the mesocyclone at $z = 0.75$ km at 2144 UTC, when the low-level vertical vorticity and circulation were not nearly as large. Both circuits comprise 10 000 parcels and have a radius of 1.5 km at the start of their respective backward integrations. The circuits are integrated backward in time to 2132 UTC. The initial altitude of the circuits results in less downward extrapolation of backward

trajectories than occurs if the circuits are backward-integrated from lower altitudes. The large number of parcels ensures that the material circuits are well resolved throughout the integration (adjacent parcels are rarely more than 25 m apart).

Circuit A approaches the low-level mesocyclone from the east in the 2132–2148 UTC period (Figs. 1a,c,d), with part of the circuit approaching from the warm sector to the east-southeast (the segment extending from a point roughly halfway between I and J to near A in Fig. 1a), and most of the circuit passing through the southern periphery of the forward-flank precipitation region to the east-northeast (roughly the B–I segment, per the labels in Fig. 1a). The former path is almost straight into the updraft (e.g., parcel J's trajectory in Fig. 2). The latter path is more tangential as this flow turns southward (while subsiding) around the west side of the circulation (e.g., parcel B's trajectory in Fig. 2). The pressure field retrieved from the three-dimensional velocity fields [following the technique outlined by Gal-Chen (1978) and Hane and Ray (1985)][8] reveals a mesohigh in the outflow and mesolow in the inflow, and the resulting horizontal pressure-gradient force bends the flow from the forward flank cyclonically around the west side of the mesocyclone. The horizontal pressure-gradient force has a negligible curl.[9] Thus, the cyclonically curved flow is mainly irrotational, although parcels can acquire cyclonic vorticity as they near the mesocyclone via the "tilting in a downdraft" processes described in sections 1 and 6c.

In the far field[10] (i.e., at 2132 UTC), the diagnosed C is small (0.1–0.3×10^5 m^2 s^{-1}, depending on how the horizontal winds at the lowest grid level are handled; Fig. 1b), which implies that the environmental vorticity contributed little to the circulation of the material circuit (at most, $\sim$10%–25% of the maximum circulation acquired by the circuit, if there was no additional solenoidal generation prior to 2132 UTC). This is perhaps a surprising result, given the relatively large environmental horizontal vorticity; after all, there was sufficient vertical wind shear for supercells (Fig. 2b of Part I).

---

[8] In the course of their tests with synthetic data, Majcen et al. (2008) found that retrieved horizontal pressure fields were much more credible than retrieved horizontal buoyancy fields.

[9] The *retrieved* horizontal pressure-gradient force has zero curl because the density in the pressure-gradient force is replaced with the environmental density that is a function of z only.

[10] By "far field," we are referring to when the circuit is well upstream of the low-level mesocyclone and much larger in size than at the start of the backward integration. Much of the circuit, however, is still within the outer reaches of the forward-flank precipitation shield where light rain is falling.
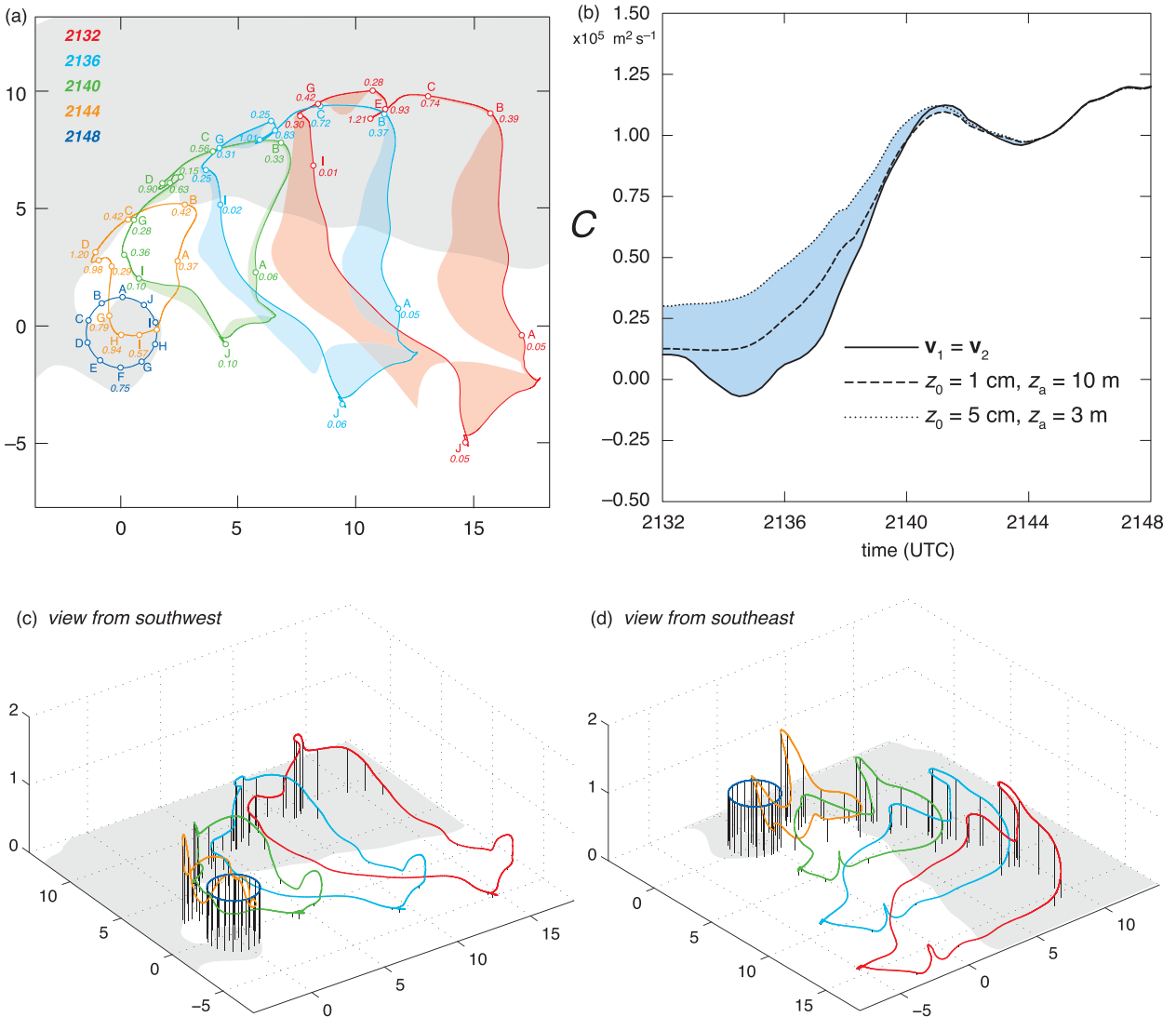
Circuit A

FIG. 1. (a) View from above of a material circuit integrated backward in time from 2148 to 2132 UTC (circuit A). The circuit comprises 10 000 parcels and is a 1.5-km-radius ring centered on the location of maximum vertical vorticity at $z = 0.75$ km at 2148 UTC. The horizontal projection of the circuit is shown every 4 min. Every 1000th parcel is indicated with a marker, and select markers are labeled with the letters A–J and altitudes in km. Where parcels go below the data horizon, winds were extrapolated (see section 3 for details). The circuits shown were computed by setting the horizontal velocity at the lowest grid level ($\mathbf{v}_1$) to the horizontal velocity at $z = 0.25$ km (the lowest grid level with data; $\mathbf{v}_2$); the color shading encompasses the horizontal projections of circuits integrated backward in time assuming roughness lengths (z_0) of 1–5 cm and anemometer levels (z_a) of 3–10 m, where downward extrapolation was required. A steady-state three-dimensional wind field was assumed from 2132 to 2142 UTC. Gray shading indicates DOW7 reflectivity factor at $z = 0.75$ km in excess of 30 dBZ. Axis labels are in km. (b) Circulation (C) about the material circuit as a function of time. The solid trace is derived from wind fields in which $\mathbf{v}_1 = \mathbf{v}_2$ was specified. The dashed and dotted traces are derived from wind fields in which $\mathbf{v}_1$ was obtained via the log wind relation, with $z_a = 10$ m and $z_0 = 1$ cm, and $z_a = 3$ m and $z_0 = 5$ cm, respectively. The blue shading encompasses the range of circulation tendencies for $z_0 = 1$–5 cm and $z_a = 3$–10 cm; it could be considered to represent the uncertainty in C owing to the downward extrapolation (the uncertainty in C unrelated to extrapolation is discussed in the appendix with the aid of synthetic data experiments). Note that no extrapolation occurs in the 2144–2148 UTC period. (c),(d) Three-dimensional perspectives of the circuits viewed from the southwest and southeast, respectively, for the analysis in which $\mathbf{v}_1 = \mathbf{v}_2$ was specified. A vertical pole is located at the position of every 500th parcel in the circuit in order to give a sense of the vertical projection of the circuit. The vertical scale is exaggerated. Gray shading indicates DOW7 reflectivity factor at 0.5 km in excess of 30 dBZ, as in (a). Axis labels are in km.
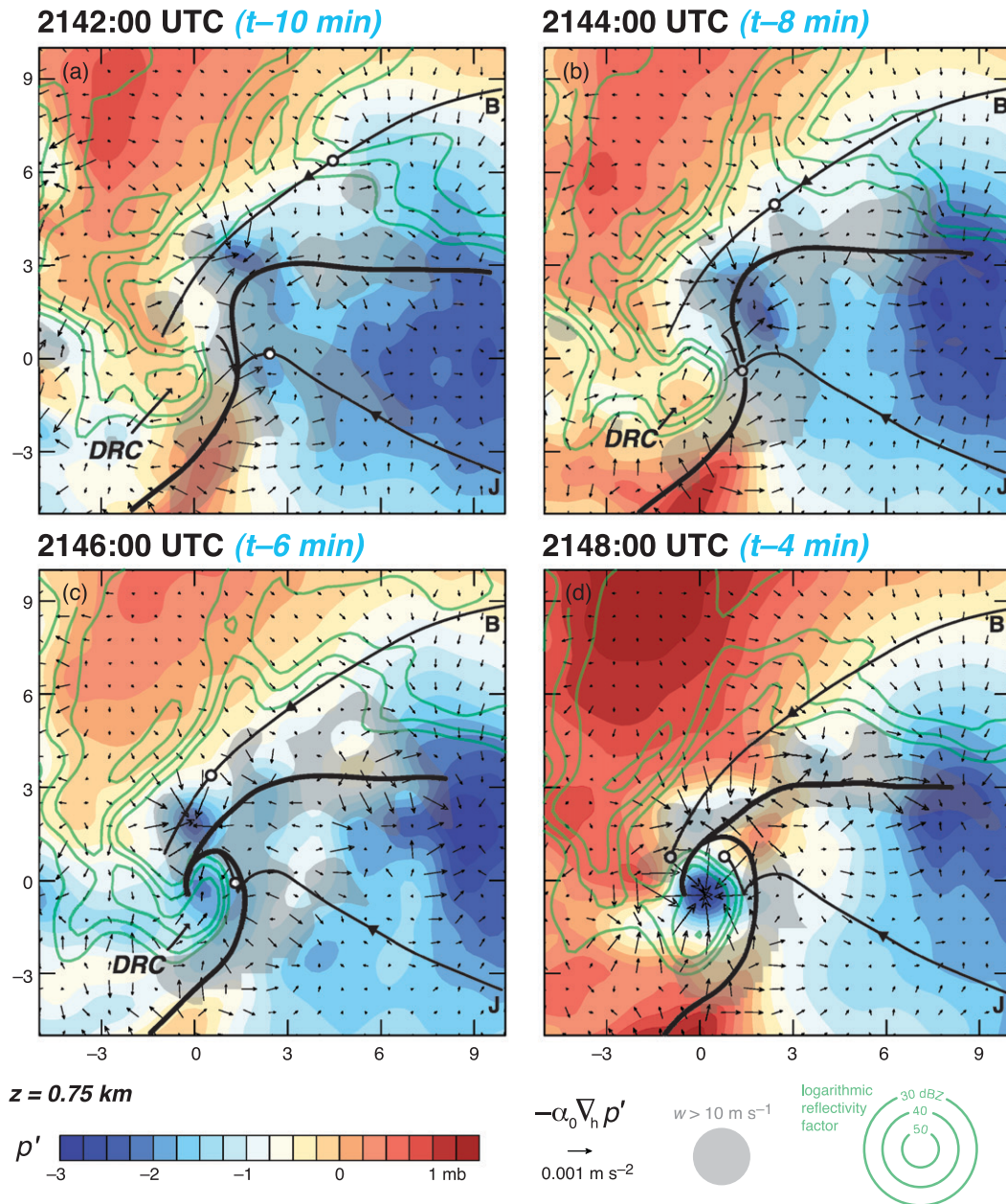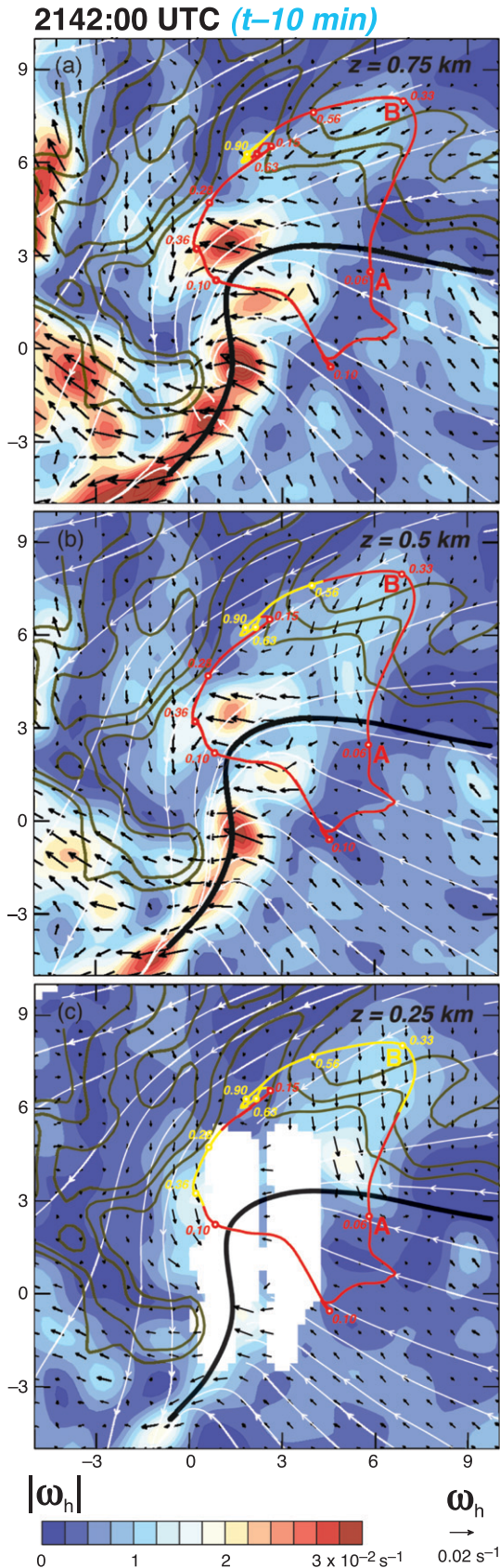
FIG. 2. Pressure perturbation (p'; color), DOW7 logarithmic reflectivity factor (green contours every 10 dBZ for reflectivity $\geq$30 dBZ), and horizontal pressure-gradient force vectors ($-\alpha_0\nabla_h p'$, where α_0 is a reference specific volume of 1.08 m^3 kg^{-1}; plotted at every third grid point using black arrows) at $z = 0.75$ km obtained from the fine ($\kappa_0 = 0.48$ km^2) dual-Doppler wind syntheses at (a) 2142:00, (b) 2144:00, (c) 2146:00, and (d) 2148:00 UTC ("$t - X$ min" indicates X min prior to tornadogenesis). Regions of strong updraft ($w > 10$ m s^{-1}) at $z = 2$ km are shaded gray. Gust fronts are indicated with heavy black lines. Axis labels are in km. Pressure perturbations are relative to the average pressure within the entire dual-Doppler domain [the southwest and northeast corners of the domain are $(-10, -10)$ and $(30, 30)$, respectively; only a subdomain is shown above]. The trajectories of parcels B and J of circuit A also are overlaid in each panel (cf. Fig. 1a). The locations of the parcels at the respective analysis times are indicated by the circular markers along the trajectories.

2142:00 UTC *(t–10 min)*

FIG. 3. Magnitude of the horizontal vorticity ($|\boldsymbol{\omega}_h|$; color shading) at 2142 UTC obtained from the fine ($\kappa_0 = 0.48$ km^2) dual-Doppler wind syntheses at heights of (a) 0.75, (b) 0.50, and (c) 0.25 km. Velocity derivatives were computed using fourth-order, centered differences, except near data boundaries where second-order, uncentered differences were used. White regions in (c) indicate missing data owing to contamination by ground clutter (see Fig. 3e in Part I). Horizontal vorticity vectors ($\boldsymbol{\omega}_h$; black) and streamlines (white) also are shown. The DOW6 reflectivity (gray) is contoured every 10 dBZ for reflectivity $\geq$30 dBZ. The subjectively analyzed gust front is indicated with the bold black line. The horizontal projection of circuit A at 2140 UTC (for the analysis in which $\mathbf{v}_1 = \mathbf{v}_2$ was specified; cf. Fig. 1a) also is shown, which is near the end of the period of most rapid circulation growth about the circuit (Fig. 1b). The location of parcels A and B are indicated, as are the heights of parcels A–J (parcels are indicated with markers along the circuit) in km. The curve is yellow along the portions that define a surface through which there is a flux of horizontal vorticity at the level of the horizontal cross section. Otherwise the curve is red. The wind field at 2140 UTC was assumed to be the same as the 2142 UTC wind field in the calculation of the trajectories comprising the circuit. Axis labels are in km.

Most of the circulation of circuit A appears to have been acquired in the 2135–2141 UTC period (Fig. 1b), which is when the circuit centroid travels roughly along the forward-flank gust front from a location ~10 km east-northeast of the vertical vorticity maximum to ~4 km northeast of the vertical vorticity maximum (note the positions of the blue and green curves plotted in Fig. 1a, which show the circuit at 2136 and 2140 UTC, respectively). In just 6 min (by 2141 UTC), C increases to 1.1×10^5 m^2 s^{-1}.

The northern portion of circuit A (the segment B–G in Fig. 1a) has a peak altitude of 1.1 km and, as a result, a significant vertical projection during the 2135–2141 UTC period (this is perhaps best visualized in Fig. 1c). (The vertical projection of the circuit is insensitive to the extrapolation of winds to the lowest grid level, because the parcels responsible for the large vertical projections never drop below the data horizon.) The geometry of the circuit is such that there is a flux of large ($>10^{-2}$ s^{-1}) southward-directed horizontal vorticity through the vertical projection, which has the correct orientation to contribute to positive circulation. Most of the horizontal vorticity flux is at $z = 0.25$ km (Fig. 3c; note especially the differences among the three panels of Fig. 3). The southward-directed (predominantly crosswise) vorticity has an orientation that is more consistent with the origin of the horizontal vorticity being surface drag (easterly winds in the forward flank that increase with height) than baroclinic vorticity generation. If the horizontal vorticity at this level were dominated by baroclinic

generation, we would expect the orientation of the vorticity to be much more toward the southwest, given that baroclinic vortex lines tend to reside in equivalent potential temperature θ_e surfaces, at least if θ_e is being conserved (RK85; Davies-Jones et al. 2001). The θ_e contours have a southwest–northeast orientation (Fig. 17f of Part I), similar to the orientation of the virtual potential temperature θ_v contours (Fig. 4). The forward-flank horizontal vorticity at higher levels (e.g., $z = 0.75$ km) in proximity to the circuit in the 2135–2141 UTC period points toward the southwest [e.g., near (6, 6) in Fig. 3a], that is, in a direction more consistent with baroclinic vorticity generation; however, this vorticity does not contribute to the circulation of the circuit because it lies above the circuit.

The track and evolution of circuit B (Fig. 5), 4 min prior to circuit A, is similar to that of circuit A in all but the last 4 min of the integration of the trajectories (the times series of C for both circuits are shown in Fig. 5b), although much of this similarity is likely forced by the assumption of a steady wind field prior to 2142 UTC. For example, virtually all of the increase in C occurs on the southern fringe of the forward-flank precipitation region, 4–10 km northeast of the vertical vorticity maximum, as was the case for circuit A. In the far field, C is ~10%–30% of the maximum C acquired by the circuit (Fig. 5b), depending on how the horizontal winds at the lowest grid level are handled.

What is strikingly different between circuits A and B, however, is the trend in C in the last 4 min of the approach of the circuits to their final positions encircling the vertical vorticity maximum at $z = 0.75$ km (i.e., the trend in C in the 2144–2148 and 2140–2144 UTC periods for circuits A and B, respectively). In the 2144–2148 UTC period, C increases to 1.2×10^5 m^2 s^{-1} along circuit A, following a small drop in C from 2141–2144 UTC (Fig. 1b). However, for circuit B, C *decreases* in the 2140–2144 UTC period to 0.7×10^5 m^2 s^{-1} (Fig. 5b). At 2142 UTC, parcels A, B, and G on circuit B are all at the same height, while parcels H, I, and J are only slightly higher (Fig. 6b); that is, $\Delta z \approx 0$ for segment G–B (here Δz is the vertical dimension of the segment). From (1), and because parcel E is at the high point of circuit B, it seems likely that C is decreasing at this time owing to parcels on segment B–E ($\Delta z > 0$) being more negatively buoyant than parcels on segment E–G ($\Delta z < 0$). Another key difference between circuits A and B is that *a larger fraction of the parcels comprising circuit A originate in the outflow*, which is a manifestation of the low-level mesocyclone becoming occluded in the 2146–2148 UTC period. This point will be discussed further in sections 5 and 6b. Material circuits tracked in the Arcadia, Oklahoma, supercell (17 May 1981) by
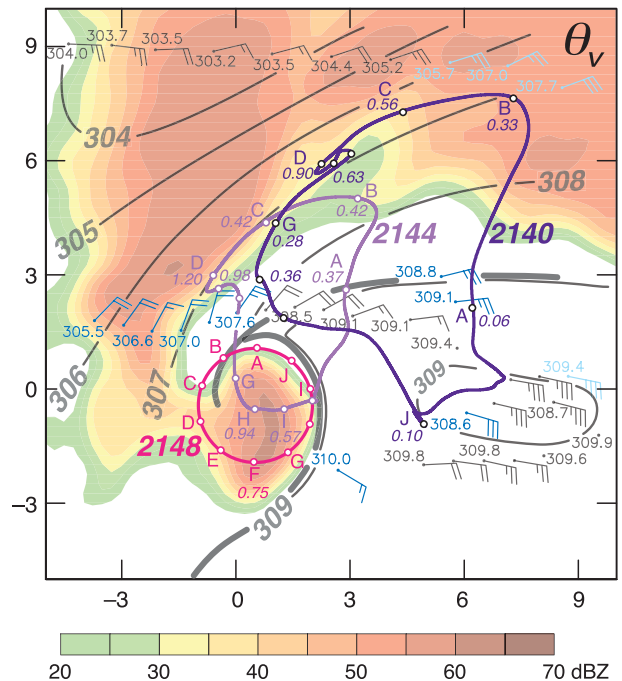

FIG. 4. Manual analyses of virtual potential temperature (θ_v; K) derived from mobile mesonet observations obtained between 2143 and 2153 UTC (gray contours). The observations are plotted relative to the storm at 2148 UTC using time-to-space conversion (cf. Fig. 17e of Part I). Station models depict storm-relative winds (half barb = 2.5 m s^{-1}; full barb = 5 m s^{-1}) and θ_v values. Observations within 2.5 min of 2148 UTC are gray; observations obtained more than 2.5 min after (before) 2148 UTC are dark (light) blue. The objectively analyzed logarithmic reflectivity factor (dBZ) from the DOW7 radar at $z = 0.5$ km is displayed in the background. The gust fronts derived from the dual-Doppler wind synthesis are indicated with heavy gray lines. Axis labels are in km. The horizontal projections of circuit A at 2140, 2144, and 2148 UTC ($\mathbf{v}_1 = \mathbf{v}_2$ specified; cf. Fig. 1a) also are shown in dark blue, purple, and magenta, respectively (2140 UTC is near the end of the period of most rapid circulation growth about the circuit; Fig. 1b). Altitudes of select parcels along the circuit are indicated in km.

Dowell and Bluestein (1997; see their Fig. 17) suggested a similar change in trajectories as tornadogenesis neared.

Although we do not know the details of the three-dimensional buoyancy field, it appears as though the buoyancy field encountered by circuit B is decidedly unfavorable in the last 4 min of circuit B's approach to its final position, given that the circulation of the material circuits, in the inviscid limit, only can be changed by baroclinic vorticity generation (more precisely, by baroclinically generated horizontal vorticity that has a component normal to a hypothetical membrane stretched over the circuit). Circuit B's geometry and the diagnosed DC/Dt in those final minutes (Fig. 6b) seem consistent with the likely orientation of the buoyancy
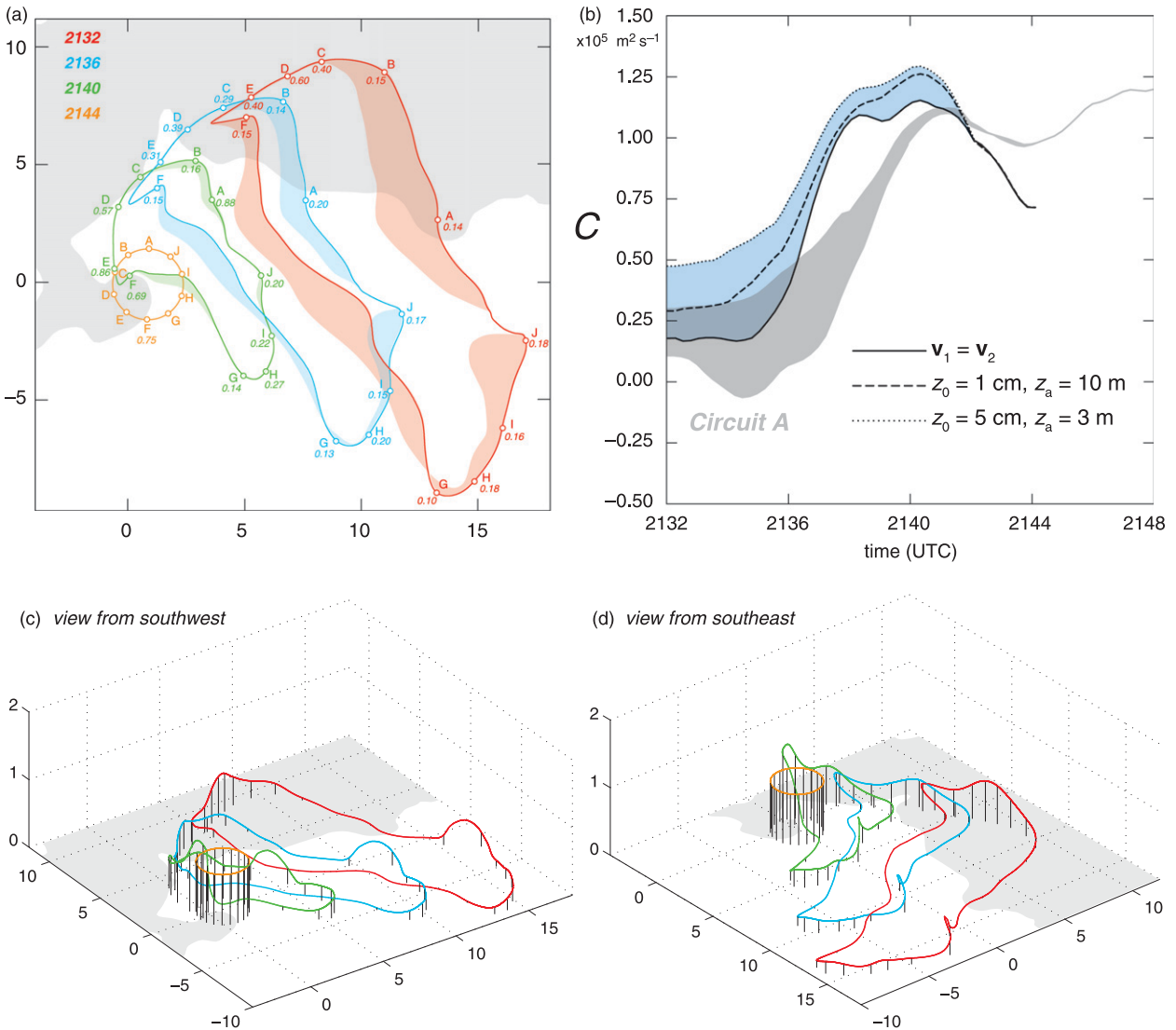
Circuit B

FIG. 5. As in Fig. 1, but for a material circuit integrated backward in time from 2144 to 2132 UTC (circuit B). The circuit is a 1.5-km-radius ring centered on the location of maximum vertical vorticity at $z = 0.75$ km at 2144 UTC. The gray trace in (b) is the time series of circulation for the material circuit shown in Fig. 1.

isopleths in the hook echo region (Fig. 4). For example, the vertical projection at 2142 UTC from C–G (note the blue circuit in Fig. 6b) would be pierced from the northeast by southwestward-pointing baroclinic vorticity generation ($\nabla \times B\mathbf{k}$) vectors if the buoyancy isopleths above the surface have an orientation not wildly different from that of the virtual isentropes analyzed at the surface (Fig. 4), yielding $DC/Dt < 0$. In contrast, it can be inferred from the diagnosed DC/Dt that circuit A does not experience such adversity. Unfortunately, similarly simple visualizations relating horizontal vorticity generation to the surface defined by circuit A are

precluded by the "unfriendly" geometry of the circuit in its last few minutes of approach to the low-level mesocyclone region (note the altitude variations along segment C–A in Fig. 6a), and the likely complexity of the buoyancy field along the circuit in the 2146–2148 UTC period (e.g., the long D–J segment is in a region characterized by large reflectivity gradients and potentially large gradients of hydrometeor mass). However, *the "smoking gun" associated with the dramatic differences in the circulation tendencies of circuits A and B appears to be the DRC* documented in section 4a of Part I (Fig. 12 of Part I).
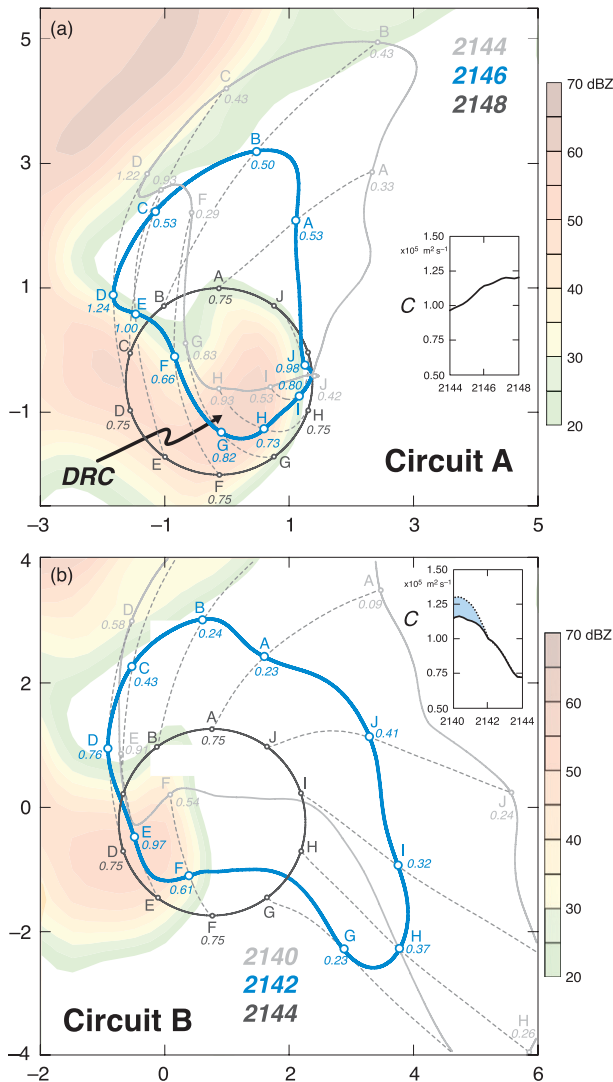
FIG. 6. (a) Zoomed-in view from above of circuit A at 2144 (light gray), 2146 (blue), and 2148 UTC (dark gray) (cf. Fig. 1a). Every 1000th parcel is indicated with a marker, and select markers are labeled with the letters A–J and altitudes in km. Dashed gray lines indicate parcel trajectories. Color shading indicates DOW7 reflectivity factor at $z = 0.75$ km at 2146 UTC. The inset shows the time series of circulation during this period. (b) As in (a), but for circuit B at 2140 (light gray), 2142 (blue), and 2144 UTC (dark gray) (cf. Fig. 5a). Color shading indicates DOW7 reflectivity factor at $z = 0.75$ km at 2142 UTC. Axis labels are in km.

Because the DRC only arrives at low levels at approximately the time that circuit B reaches its final position (an exact time cannot be given because it depends on the reflectivity isosurface being considered; the 55-dBZ isosurface shown in Part I's Fig. 12 reaches $z = 0.75$ km between 2146 and 2148 UTC), there is little interaction between circuit B and the DRC (Fig. 6b). In contrast, a long segment of circuit A passes through the

DRC as the circuit is converged upon its final position (Fig. 6a). The differences in C between circuits A and B at 2148 and 2144 UTC, respectively, are primarily due to differences in $\mathbf{v} \cdot \mathbf{dl}$ along the A–G segment of the circuits (Fig. 7),[11] which, for circuit A, is the segment in proximity to and within the hook echo and DRC (Fig. 6a). Because the parcels are equally spaced on a circle, $\mathbf{v} \cdot \mathbf{dl}$ is proportional to a parcel's angular momentum relative to the center of the circle (see section 5). It is also evident from the profile of $\mathbf{v} \cdot \mathbf{dl}$, as well as past simulations (e.g., RK85, DJB93), that the warm-sector air contributes little to the low-level circulation.

5. Evolution of angular momentum within the low-level mesocyclone

In this short section we complement the Lagrangian analysis of circulation about material circuits that converge upon the low-level mesocyclone (section 3a) with an analysis of angular momentum within a fixed region surrounding the low-level circulation center. We wish to investigate how low-level angular momentum was influenced by the occlusion of the low-level mesocyclone that coincided with the intensification of rotation during the 2142–2148 UTC period (note the evolution of the gust fronts in Fig. 2).

The angular momentum of a parcel with respect to the circulation axis is

$$M = \mathbf{k} \cdot \mathbf{r} \times \mathbf{v}, \qquad (3)$$

where $\mathbf{r}$ is a position vector from the circulation axis. The evolution of the M integrated over a control disk having an area A, $\int M \, dA$ (proportional to area-averaged M), is governed by

$$\frac{\partial}{\partial t} \int M \, dA = -\oint u M \, dl - \int \frac{\partial (wM)}{\partial z} \, dA, \qquad (4)$$

where u is the radial velocity (negative toward the circulation axis), the line integration is performed around

---

[11] To determine which portions of the circuits are responsible for the circulation differences, the best we can do is compare $\mathbf{v} \cdot \mathbf{dl}$ for two identically shaped circuits having constant $|\mathbf{dl}|$, as is done in Fig. 7. Although it is tempting to compare, at different times, $D(\mathbf{v} \cdot \mathbf{dl})/Dt$ as a function of location along the circuits, such an analysis is unenlightening because of the variation in $|\mathbf{dl}|$ in time, following a circuit (the distance between parcels within the circuits generally decreases as the circuits approach the low-level mesocyclone, given that the circuits experience mean convergence). Although $\mathbf{dl}$ is just an infinitesimal element of a circuit, the circuits are discretized, with $\Delta \mathbf{l}$ being obtained from the relative positions of adjacent parcels within the circuits.
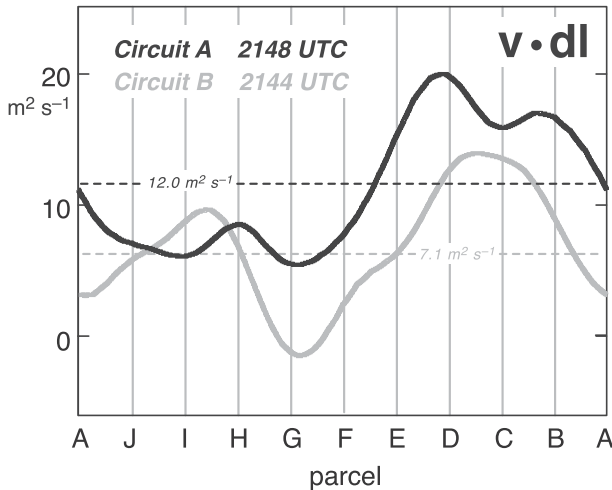
FIG. 7. Azimuthal profiles of $\mathbf{v} \cdot \mathbf{dl}$ for circuits A (black) and B (gray) at 2148 and 2144 UTC, respectively (i.e., at the times when the circuits are circles centered on the vorticity maxima at $z = 0.75$ km). The labels on the abscissa are the parcels A–J (cf. Figs. 1a and 5a). The mean $\mathbf{v} \cdot \mathbf{dl}$ for each circuit is indicated with a dashed line; the mean times the number of parcels comprising the circuits (10 000) gives the circulation ($C = \oint \mathbf{v} \cdot \mathbf{dl}$) about the circuits (cf. Figs. 1b and 5b).

the perimeter of the control disk, and the terms on the rhs represent the integrated radial and vertical fluxes of angular momentum, respectively.

We evaluated each term in (4) within a 2-km-radius circle centered on the circulation at $z = 0.75$ km from 2142 to 2148 UTC (Fig. 8). The $(\partial/\partial t) \int M \, dA$ trend was computed from the M field shown in Fig. 9 via second-order centered differencing from 2144 to 2148 UTC, and second-order uncentered differencing at 2142 UTC [this is the time of the first Doppler-on-Wheels (DOW)6–DOW7 dual-Doppler wind synthesis]. The M fluxes on the rhs of (4) were evaluated using the winds relative to the circulation center, as opposed to the grid-relative winds; a small grid-relative drift of the circulation center is evident in Fig. 9. The confidence in the calculation of the terms in the angular momentum budget is highest from 2142 to 2146 UTC, when the independently calculated $(\partial/\partial t) \int M \, dA$ and $-\oint uM \, dl - \int [\partial(wM)/\partial z] \, dA$ are in excellent agreement (cf. the dashed black and solid gray lines in Fig. 8).

The integral $\int M \, dA$ increases throughout the 2142–2148 UTC period, and most rapidly at 2146 UTC (Figs. 8 and 9). The vertical flux term is negative throughout the 2142–2148 UTC period (Fig. 8) but becomes steadily less negative from 2144 to 2148 UTC. Within the warm sector, $-\partial(wM)/\partial z < 0$ (Fig. 10); thus, the integrated vertical flux of angular momentum increases as occlusion occurs (after 2144 UTC) and only a small bit of warm-sector air remains within the control disk.
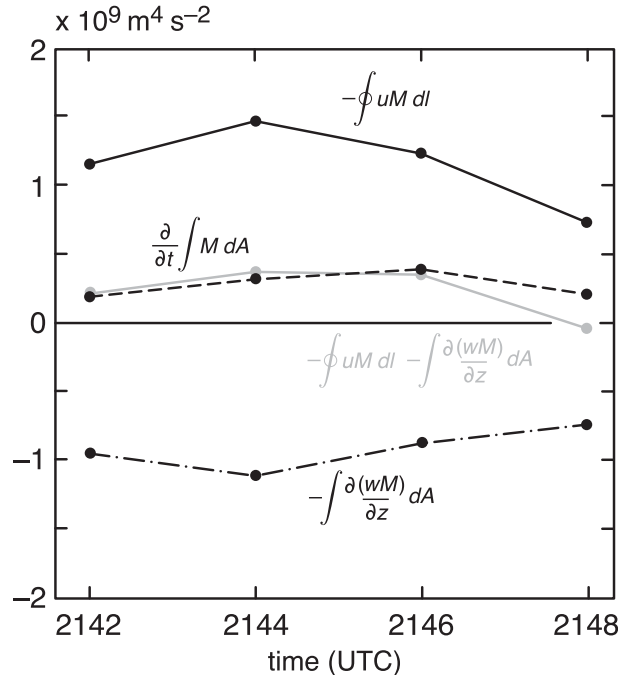

FIG. 8. Evolution of the rate of change of angular momentum integrated over the control disk [$(\partial/\partial t) \int M \, dA$; dashed line], the integrated vertical angular momentum flux {$-\int [\partial(wM)/\partial z] \, dA$; solid line}, the integrated radial angular momentum flux ($-\oint uM \, dl$; dash–dotted line), and the sum of the integrated vertical and radial angular momentum fluxes {$-\oint uM \, dl - \int [\partial(wM)/\partial z] \, dA$; gray line}.

Rising motion in the warm-sector air transports lower-M air from lower elevations upward, which is detrimental to low-level rotation. The elimination of the warm-sector air from the near surroundings reduces this negative vertical flux of angular momentum. The increase in M within the control disk as warm-sector air is replaced by outflow air is consistent with the differences between circuits A and B in section 4 (recall that circuit A comprised less warm-sector air than circuit B).

From 2142 to 2146 UTC, the radial flux imports M into the control disk increasingly faster than the vertical flux is exporting M out of the disk per the trend in $\partial/\partial t(\int M \, dA)$ (Fig. 8). There is a positive radial flux through the southeast–northwest arc of the circle during this period. From 2142 to 2144 UTC, the radial flux of angular momentum is negative along the west-southeast arc of the circle (Figs. 9a,b), although the radial influx through the rest of the circle is sufficiently positive that $-\int uM \, dl$ spikes at 2144 UTC (Fig. 8). The negative radial flux along the southern arc of the circle becomes decidedly less negative by 2146 UTC; the low-M air to the south of the circulation center at 2142 and 2144 UTC
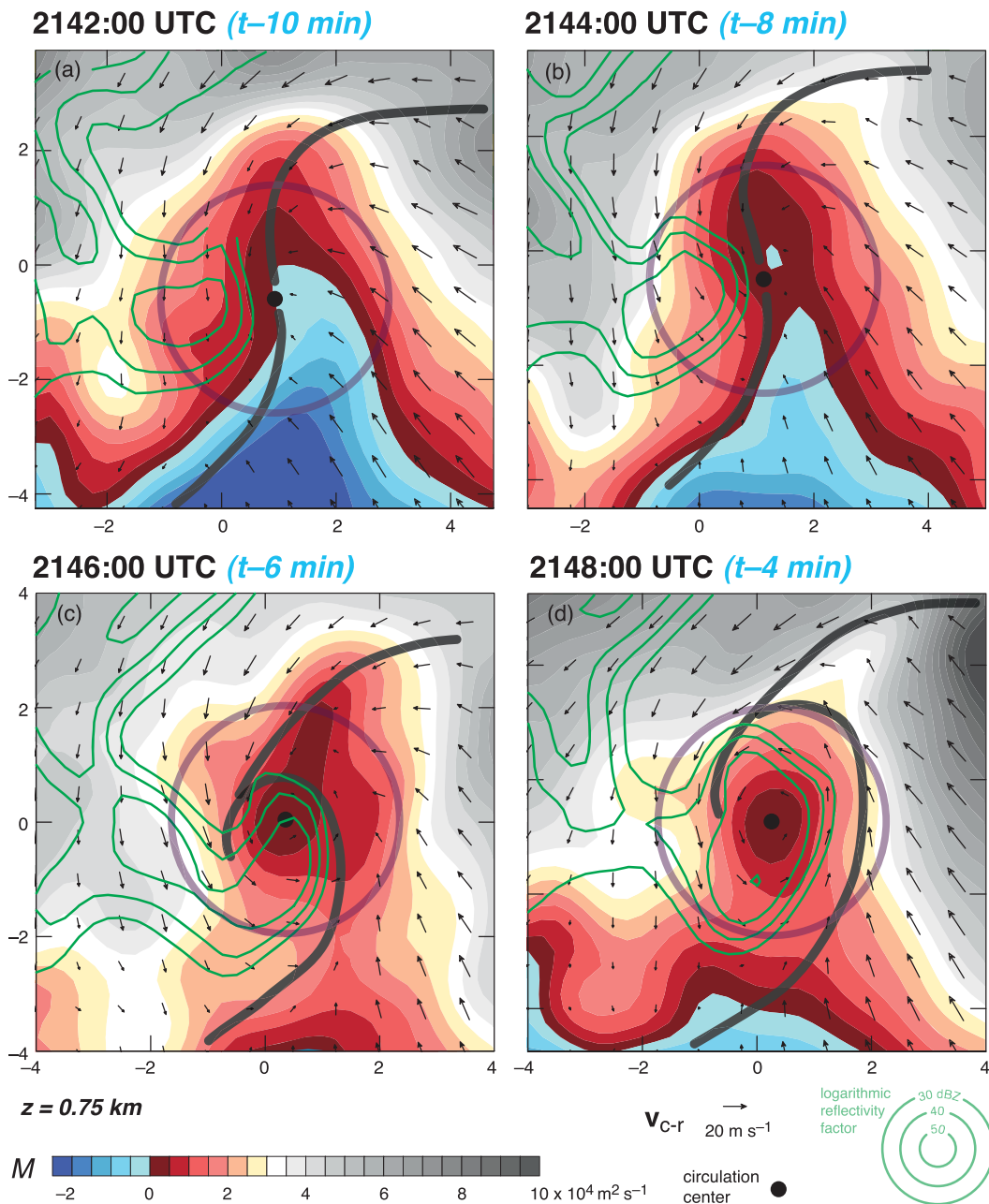
FIG. 9. Angular momentum (M; color) relative to the circulation center (black dot), DOW7 logarithmic reflectivity factor (green contours every 10 dBZ for reflectivity $\geq$30 dBZ), and circulation-relative wind vectors ($v_{c\text{-}r}$; plotted at every fifth grid point using black arrows) at $z = 0.75$ km obtained from the fine ($\kappa_0 = 0.48$ km^2) dual-Doppler wind syntheses at (a) 2142:00, (b) 2144:00, (c) 2146:00, and (d) 2148:00 UTC. (The circulation-relative winds used to compute M differ from the grid-relative winds by 1–3 m s^{-1}; the grid was translated at a constant speed to match the mean motion of the mesocyclone at $z = 1.5$ km between 2130 and 2148 UTC.) Gust fronts are indicated with heavy gray lines. Axis labels are in km. The 2-km-radius circle centered on the circulation, within (about) which vertical (radial) momentum fluxes were computed (cf. Fig. 8), also is overlaid in each panel.

is "blocked out" of the occluding mesocyclone by 2146 UTC [e.g., near $(1, -2)$ in Fig. 9c].

At 2148 UTC the radial influx and vertical efflux of angular momentum are approximately equal (Fig. 8).

The radial influx decreases to roughly half its maximum value at this time, a result of little radial inflow through a large arc of the circle (Fig. 9d). The downward trend in the radial influx of angular momentum at $z = 0.75$ km
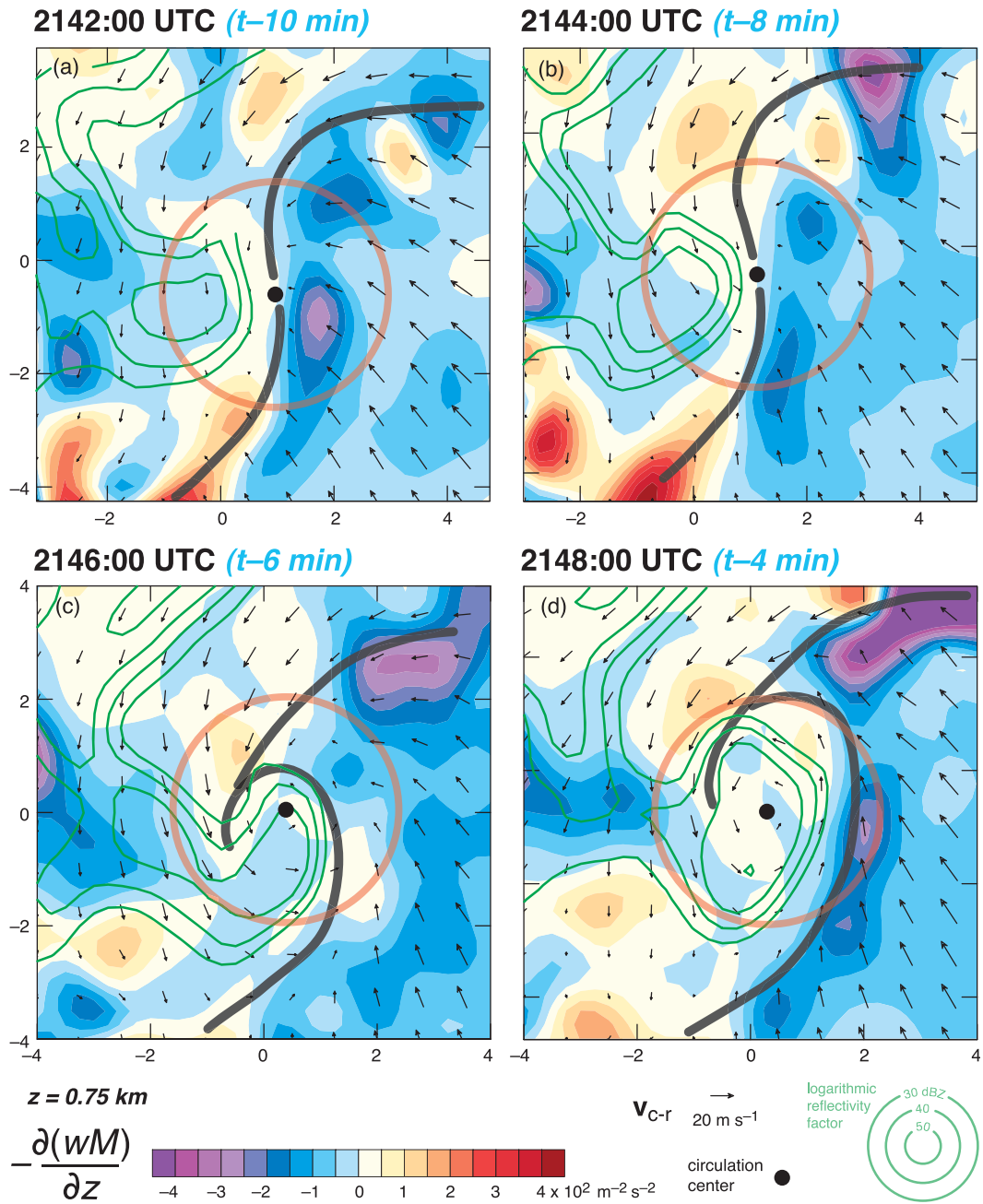
FIG. 10. Vertical flux of angular momentum [$-\partial(wM)/\partial z$; color], DOW7 logarithmic reflectivity factor (green contours every 10 dBZ for reflectivity $\geq$30 dBZ), and circulation-relative wind vectors ($\mathbf{v}_{c\text{-}r}$; plotted at every fifth grid point using black arrows) at $z = 0.75$ km obtained from the fine ($\kappa_0 = 0.48$ km^2) dual-Doppler wind syntheses at (a) 2142:00, (b) 2144:00, (c) 2146:00, and (d) 2148:00 UTC. The angular momentum is defined relative to the circulation center (black dot). (The circulation-relative winds used to compute M differ from the grid-relative winds by 1–3 m s^{-1}; the grid was translated at a constant speed to match the mean motion of the mesocyclone at $z = 1.5$ km between 2130–2148 UTC.) Gust fronts are indicated with heavy gray lines. Axis labels are in km. The 2-km-radius circle centered on the circulation, within (about) which vertical (radial) momentum fluxes were computed (cf. Fig. 8), also is overlaid in each panel.

in the 2144–2148 UTC period could be a consequence of the inflow to the intensifying vortex becoming shallower in time [e.g., by the time a vortex attains tornado strength, its inflow typically is confined to the lowest 50–100 m (e.g., Lewellen et al. 1997), which is below the level of most radar observations, the exception being radar observations obtained at very close range (within ~1 km)].

6. Discussion

a. The generation of circulation within the forward-flank baroclinic zone

The FFD has been present in long-standing conceptual models of supercells (e.g., Lemon and Doswell 1979; Doswell and Burgess 1993), and the horizontal buoyancy gradient along its southern periphery has been found to be dynamically important, at least in numerical simulations of supercells, by generating horizontal vorticity baroclinically (e.g., Klemp and Rotunno 1983; RK85; DJB93; Adlerman et al. 1999). In the Goshen County storm, horizontal vorticity was enhanced in a broad swath north of the forward-flank gust front [e.g., in the region extending from roughly (0, 3) to (9, 6) in Fig. 3]. The forward-flank horizontal vorticity was mainly crosswise at $z = 0.25$–0.50 km (Figs. 3b,c) and streamwise above that (Fig. 3a). One might expect a general tendency for the horizontal vorticity in the forward flank to be streamwise (indeed, it is, in numerical simulations, at least those using a free-slip lower boundary condition), because storm-relative streamlines approaching the updraft from the forward flank are generally aligned with the buoyancy isopleths. Near the surface, where the effects of friction are most important, one might imagine that the vorticity also could have a significant crosswise component.

The evolution of circuits A and B and their circulation within the forward flank of the Goshen County storm (Figs. 1 and 5) share some similarities with the material circuit tracked in RK85's simulation (see their Figs. 11 and 12). The RK85 simulation was initialized with an environment having unidirectional (westerly) wind shear. A plane of symmetry is present at $y = 0$. The horizontal vorticity at $y = 0$ is constrained by symmetry to be in the y direction. Because the meridional wind vanishes at the plane of symmetry, some of the backward trajectories climb upward beside the plane (see their Fig. 11). Initially, the horizontal vorticity is crosswise and points northward owing to the environmental shear, but it later turns southward in the region ahead of the coldest part of the cold pool, where $\partial B/\partial x > 0$. Thus, the baroclinically generated vorticity also is crosswise, at least in the

outer parts of the forward flank, and the vortex lines penetrate the surface bounded by the circuit in the right way to yield positive circulation. Although the environmental hodograph in the inflow of the Goshen County supercell possesses approximately southerly shear in the lowest 0.4 km, the vertical wind shear is roughly unidirectional and westerly above that altitude (Fig. 2b of Part I). Similarly, the vertical projections of circuits A and B also are roughly west–east oriented in the forward flank, though shallower than the projection of the circuit in the RK85 simulation, and also threaded by approximately crosswise vortex lines that point southward (Fig. 3c). The circulation increase about the material circuits between the far field and mesocyclone region in both the RK85 simulation and Goshen County storm is $\sim 1 \times 10^5$ m^2 s^{-1} (cf. Fig. 1b herein and RK85's Fig. 12).

There are some noteworthy differences between the Goshen County storm and the RK85 simulation. The first concerns the orientation of the horizontal vorticity responsible for the circulation about the circuits in the far field. In the RK85 simulation, the horizontal vorticity is aligned with the isentropes (with cold air to the right), which is the direction one would expect if the horizontal vorticity tendency is dominated by baroclinic vorticity generation. However, in the Goshen County storm, as noted in section 4, the horizontal vorticity at $z = 0.25$ km points well to the left of the orientation we would expect if baroclinic vorticity generation dominated the tendency, at least in the region in which the horizontal vorticity contributes to large positive circulation (e.g., in the region ~ 8 km northeast of the circulation center; Fig. 3c). Although the forward-flank horizontal vorticity is much more streamwise at $z = 0.75$ km (and above), these vortex lines do not thread the surface defined by the material circuit (Fig. 3a). Surface drag or finite-differencing errors might be affecting the orientation of the horizontal vorticity at $z = 0.25$ km (the vertical wind shear at $z = 0.25$ km was obtained from a one-sided, albeit second-order, finite-difference approximation). We also cannot easily say to what extent contaminated raw radial velocities infiltrated the analysis of the horizontal vorticity here. Considerable editing of the raw radial velocity data was required in this region (Fig. 3c; also see Figs. 3d–f of Part I); both the resulting data holes and *unedited* data that have been biased by ground targets can adversely affect the objective analysis and subsequent wind synthesis.

Another difference between the material circuits in the Goshen County storm and the RK85 simulation is the circulation in the far field. In the Goshen County storm, the far-field circulation of both circuits A and B, albeit small, is at least positive (Figs. 1b and 5b). In

the RK85 simulation, the far-field circulation is negative. The difference is likely due to the fact that the Goshen County environment had southwestward-pointing horizontal vorticity in the lowest 0.3 km (Fig. 2b of Part I), whereas the RK85 environment has northward-pointing horizontal vorticity. Given the circuit geometries, southwestward-pointing (northward-pointing) horizontal vorticity would contribute toward positive (negative) circulation. Wicker (1996) found that the orientation of the low-level environmental horizontal vorticity, relative to the orientation of the horizontal vorticity that would be generated baroclinically in the forward flank, can influence the strength of low-level mesocyclones in simulated supercells. His findings might be tied to the flux of environmental vortex lines through the surfaces defined by material circuits backward-integrated from the mesocyclone region into the environment.

The most obvious difference between the material circuits in the Goshen County storm and RK85 simulation is the *rate* at which circulation about the circuits increases. Although the total circulation changes from the far field to the mesocyclone region ($\sim 1 \times 10^5$ m^2 s^{-1}) are comparable, the circulation generation rate diagnosed from the dual-Doppler wind syntheses of the Goshen County storm is considerably faster than in the RK85 simulation (wherein the C increase occurs over 25 min, per RK85's Fig. 12), despite the outflow of the RK85 simulated storm being more negatively buoyant than the outflow of the Goshen County storm (cf. Fig. 4 and RK85's Fig. 18b).

From Bjerknes' theorem, the increase in circulation ΔC during time Δt is roughly $(g/\theta_0)\,\Delta\theta_\rho \Delta z \Delta t$, where Δz is the peak height difference on the circuit, θ_0 is a representative environmental potential temperature, and $\Delta\theta_\rho$ is the typical difference in density potential temperature between the "up" part of the circuit and "down" part. For circuit A, for $\Delta t = 360$ s (i.e., 2135–2141 UTC per Fig. 1b), $\Delta z = 1000$ m (per the altitude of parcel D at 2136 UTC; Fig. 1a), and $\Delta\theta_\rho = 6$ K (per the $\sim$3-K θ_v differential observed by the mobile mesonet at the surface across the horizontal projection of circuit A at 2140 UTC in Fig. 4, with another 3 K—or the equivalent of a hydrometeor mixing ratio of roughly 10 g kg^{-1}— added to the θ_v differential to account for the effect of hydrometeors on the θ_ρ differential), $\Delta C \sim 0.7 \times 10^5$ m^2 s^{-1}. Although this estimated increase falls short of the diagnosed $\sim 1 \times 10^5$ m^2 s^{-1} increase in circulation about circuit A (Fig. 1b), the discrepancy probably should be regarded as small given the large uncertainty in the contribution of hydrometeors to $\Delta\theta_\rho$, errors in the dual-Doppler analysis (the results of synthetic data experiments are presented in the appendix), the crudeness of the estimate $\Delta C \approx (g/\theta_0)\Delta\theta_\rho \Delta z \Delta t$, and the uncertainty in

the treatment of the horizontal wind at the lowest grid level [e.g., when the horizontal winds at the lowest grid level are obtained from (2) by assuming $z_0 = 5$ cm and $z_a = 3$ m, the circulation increase in the forward flank is 0.8×10^{-5} m^2 s^{-1} (dotted trace in Fig. 1b)—that is, a closer match to the estimated ΔC].

Although we have low confidence that a real discrepancy exists between the circulation trends displayed in Figs. 1b and 5b and the circulation changes estimated from Bjerknes' theorem using the limited available thermodynamic observations (e.g., Fig. 4), we cannot exclude the possibility that surface drag contributed positively to the circulation tendency. This effect was absent from the RK85 simulation (among others), which employed a free-slip lower boundary condition. The horizontal vorticity at $z = 0.25$ km had a large crosswise component and was directed at a large angle across the θ_v (Fig. 4) and θ_e contours (Fig. 17d, Part I). Its orientation, if it can be believed in light of the concerns expressed earlier in this section, would be consistent with a strong influence from surface drag, and it was these southward-pointing vortex lines that contributed most to the vorticity flux through the surface defined by the material circuit (Fig. 3c). Given typical data horizons and the accumulation of errors that accompany calculations involving multiple derivatives (one would need to assess variations in eddy viscosity along the circuit), it is unlikely that observations alone will be able to quantify this effect.

b. The role of the DRC

What was the role of the DRC? Our analysis does not reveal the DRC to be a significant source of circulation for the low-level mesocyclone and incipient tornado, given the circulation tendency analyzed about circuit A (Fig. 1b); that is, circuit A acquires most of its circulation in the forward flank of the storm prior to reaching the vicinity of the DRC. Although we do not have observations of the three-dimensional buoyancy field, the differences in the evolution of circulation about circuits A and B in the last 4 min of their approach to their final positions encircling $\zeta_{\max}$ imply that the DRC was associated with a significant alteration of $\oint B\,dz$. We are confident in the differences in the circulation tendency in these last 4 min of approach to the low-level mesocyclone, given that none of the 10 000 trajectories of circuit A (circuit B) are extrapolated in the 2144–2148 UTC (2142–2144 UTC) period (some small amount of downward extrapolation is required in the 2140–2142 UTC period for circuit B, though 95% of the circuit remains above $z = 0.20$ km). The circulation changes experienced by the circuits in the vicinity of the DRC are

relatively small compared with the large amount of circulation generated in the forward flank, presumably because the circuits spend much more time in the forward flank than in the hook echo region.

As noted in section 4, circuit B's circulation decreases in the last 4 min of its approach to its final position, which occurs prior to the arrival of the DRC at low levels. Curiously, a similar downward trend is present in the circulation of the material circuits in the simulations of RK85 (note the trend in C from 87 to 90 min in their Fig. 12), DJB93 (note the trend in C during $t = 42$–50 min in their Fig. 7), and Nowotarski et al. (2011; note the trend in C in the "control" simulation from 81 to 85 min in their Fig. 17). An exploration of the dynamics behind this recurring negative circulation tendency is beyond the scope of this paper (it likely has something to do with how the circuits flatten out), but in the Goshen County storm, it appears as though the DRC was associated with alterations of $\oint B\,dz$ such that circuits approaching $\zeta_{\max}$ retained (and slightly increased) the circulation they had acquired in the forward flank. Thus, we view the FFD as being the primary *source* of circulation, and the DRC as being an important *modulator* of circulation. We believe this perspective is consistent with the observation that a cyclonic/anticyclonic vorticity couplet, joined by arching vortex lines (the vortex line configuration suggests the lines were baroclinically produced, as discussed in Part I), straddled the hook echo *well before* the DRC developed (e.g., Figs. 6b, 8a–c, and 10 in Part I).

We have deliberately avoided claims about the extent to which the DRC modified the buoyancy field; we only can say that the DRC was associated with modifications of $\oint B\,dz$. Although it is likely that the DRC had at least some effect on the three-dimensional buoyancy field west and south of the low-level mesocyclone (for no other reason than that a change in the hydrometeor field is likely to be associated with a change in the buoyancy field), another possible role of the DRC might have been its modification of the flow (recall from section 4 that a larger fraction of parcels originated in the outflow for circuit A than for circuit B, and recall from section 5 that the M within the fixed control disk increased as warm-sector air was replaced by outflow air). *Did the DRC promote the occlusion of the low-level mesocyclone that ultimately resulted in the net increase in the mesocyclone's area-averaged angular momentum described in section 5?* The retrieved pressure field at 2144 UTC suggests a high pressure perturbation associated with the DRC [near $(0, -1.5)$ in Fig. 2b], which is associated with an enhancement of the west-to-east-directed pressure-gradient force behind the rear-flank gust front. By 2146 UTC, the rear-flank gust front becomes "wrapped up" (Fig. 2c), and the associated increase in vorticity in this region results in a low pressure perturbation beneath the DRC (i.e., the high pressure perturbation beneath the DRC was short-lived).

With low-M air blocked out of the circulation by the RFD as it wrapped around the mesocyclone (cf. Figs. 9a,b and 9c,d), subsiding moderately high-M air would be able to spiral into the circulation center. This evolution has been found in axisymmetric numerical simulations by Davies-Jones (2008), in asymmetric simulations by Kis et al. (2008), and in further work led by J. Straka at the University of Oklahoma. It also seems similar to one of Lewellen and Lewellen's (2007, p. 2187) experiments in which a quadrant of low-M air was blocked out of the circulation, leading to what they have termed *corner-flow collapse* (i.e., the inward penetration at low levels of high-M air to near the axis of rotation).

c. The relative roles of the RFD and FFD

In section 1 it was noted that baroclinic vorticity generation must occur along a descending trajectory in order for the vorticity vector to acquire a cyclonic component by the time the trajectory reaches its nadir, if the vorticity is horizontal and streamwise far upstream (DJB93; Davies-Jones et al. 2001). When a parcel begins to subside, the vorticity vector tips downward along with the trajectory owing to the $\boldsymbol{\omega} \cdot \nabla\mathbf{v}$ term in the vorticity equation—vortex lines are material lines in the absence of baroclinity (assuming inviscid flow). The presence of baroclinity during the descent, however, results in the generation of horizontal vorticity. In the words of DJB93 (p. 111), the horizontal vorticity generation forcing introduces "slippage between the (descending) fluid and vortex lines" (also see the bottom panel of their Fig. 9), and further forcing via the $\boldsymbol{\omega} \cdot \nabla\mathbf{v}$ term (e.g., upward tilting) subsequently results in the development of positive vertical vorticity along the descending trajectories. Intense stretching can further amplify the vertical vorticity near the surface.

In addition to our general interest in the relative roles of environmental and storm-generated vorticity (refer to section 1), we believe that the roles of the FFD and RFD have yet to be satisfactorily resolved. On the one hand, it might seem that the RFD is much more relevant to the DJB93 process than the FFD, because the RFD has vertical velocities an order of magnitude larger than the FFD and is associated with even larger horizontal gradients of vertical velocity (and therefore much larger vorticity tilting rates) given its closer proximity to the storm updraft. But we do not feel as though we can yet dismiss the possibility of the DJB93 process occurring within the gentle descent of the FFD. The development of only a small vertical vorticity component could be

important given the subsequent exponential intensification that is possible from stretching. The DJB93 process aside, the FFD seems to have clear importance in the generation of circulation about the material circuits that eventually converge upon the low-level mesocyclone, based on this analysis of the Goshen County storm (Figs. 1b and 5b), but also based on the circulation analyses of RK85 *and* DJB93 (DJB93's circuit acquired its circulation well upstream of the near-vicinity of ζ_{max}; see their Fig. 7). Perhaps the FFD should be viewed as the main source of circulation, with the RFD being responsible for the rapid descent of the "rear" of the circuits that allows the circuits to become horizontal at their "final" positions (Fig. 6). Alternatively, perhaps distinguishing between RFDs and FFDs is no longer fruitful, given that the RFD and FFD typically occur within one large, contiguous region of downdraft, and sometimes there may not even be two distinct downdraft maxima (e.g., Dahl et al. 2011).

7. Summary and conclusions

In this article we investigated the evolution of circulation about material circuits that converged upon the low-level mesocyclone of the 5 June 2009 Goshen County, Wyoming, tornadic supercell intercepted by VORTEX2. The analysis focused on the 2142–2148 UTC period, during which low-level rotation increased rapidly following the development of a DRC. Our goals were to investigate the relative contributions of environmental vorticity and storm-generated vorticity to the rotation of the low-level mesocyclone, and to explore the dynamical importance of the DRC.

We have high confidence in the following conclusions:

1) The low-level mesocyclone region became increasingly dominated by air parcels originating in the outflow (as opposed to the warm sector) as rotation intensified and the circulation became occluded.
2) Although the vast majority of the circulation about the material circuits that converged upon the low-level mesocyclone appears to have been acquired in the forward-flank baroclinic zone (also see our fourth conclusion), the circulation of the material circuits was modulated in the hook echo region. A circuit that arrived at the location of ζ_{max} prior to the arrival at low levels of the highest reflectivity within the DRC (circuit B) lost some of its previously acquired circulation during its final few minutes of approach to the location of ζ_{max}. In contrast, a circuit that approached the location of ζ_{max} after the highest reflectivity of the DRC had arrived at low levels (circuit A)—a significant segment of this circuit

passed through the DRC—did not experience the same adversity.
3) The area-averaged angular momentum in the near-surroundings of the low-level mesocyclone kept increasing while the mesocyclone was occluding and warm-sector air was being displaced from the near surroundings. The occlusion process reduced the overall negative vertical flux of angular momentum into the control disk centered on the low-level mesocyclone and enabled the area-averaged angular momentum to continue increasing even though the positive radial influx of angular momentum was decreasing in time.

The following conclusions are more tentative:

4) The environmental vorticity was responsible for only a relatively small amount (at most, 10%–30%) of the circulation of the material circuits that converged upon the low-level mesocyclone. Most of the circulation was acquired in the forward flank of the storm, and Bjerknes' theorem implies that baroclinity played a major role. (This finding depends on the credibility of the assumption of a steady state in the 2132–2142 UTC period and the possibility of errors in the trajectories and circulation calculation owing to ground-clutter contamination in the forward flank.)
5) The DRC promoted the occlusion of the low-level mesocyclone. (In its early stages, a high pressure perturbation was retrieved beneath the DRC, southwest of the low-level mesocyclone center. In the ensuing minutes, the rear-flank gust front rapidly occluded the circulation center, resulting in the displacement of warm-sector air from the nearby environs of the circulation center. Nonetheless, this finding remains tentative because we do not know how the storm would have evolved had a DRC not developed.)

In section 1 we stated that one of the goals of our ongoing research is to determine the roles played by environmental vorticity and storm-generated vorticity. Our analysis suggests that storm-generated vorticity was the dominant contributor to the circulation of the low-level mesocyclone. So what is the role of environmental vorticity? The fact that midlevel mesocyclone strength is only a mediocre predictor of tornadogenesis (Wakimoto et al. 2004; Trapp et al. 2005) would, on one hand, seem to imply that factors other than environmental vorticity are important. On the other hand, the magnitude of the environmental vorticity, particularly in the lowest 500–1000 m, is used somewhat skillfully to discriminate between tornadic and nontornadic supercell environments (Doswell and Evans 2003; Markowski et al. 2003;

Rasmussen 2003; Thompson et al. 2003; Craven and Brooks 2004). The latter observation suggests that environmental vorticity is relevant, but the former observation suggests that the role of environmental vorticity might be *indirect* (i.e., not simply tied to the strength of the midlevel mesocyclone that develops). Is large environmental vorticity important, especially at low levels, because its tilting establishes the base of the midlevel mesocyclone at fairly low elevations? This would give rise to a strong upward-directed perturbation pressure-gradient force at low levels that could forcibly lift negatively buoyant air (the upward-directed perturbation pressure-gradient force must be strong enough to offset the negative buoyancy of the circulation-bearing outflow air). This was shown to be an important effect in the numerical simulations of Markowski et al. (2010), although the simulations were highly idealized (e.g., dry).

An obvious shortcoming of observations is that we generally are unable to retrieve the three-dimensional wind field from dual-Doppler observations within 100–200 m of the ground, which is where the rapid transformation of anticyclonic vorticity to cyclonic vorticity along the descending trajectories of the DJB93 and Adlerman et al. (1999) simulation studies occurs (see DJB93's Fig. 8 and Adlerman et al.'s Fig. 9). Moreover, with the possible exception of rapid-scanning radars (e.g., phased-array radars), we probably do not obtain three-dimensional volumes of wind observations fast enough in regions of rapid evolution (e.g., near ζ_{max}). Trajectory and vorticity budget calculations are hampered by both data horizon limitations and rapid evolution relative to the scanning rate. We believe that it will be essential to complement observational analyses with numerical modeling studies, both idealized and ''case-study'' simulations (this includes the analysis of storms using the latest data assimilation techniques). Diagnosing the three-dimensional buoyancy field and quantifying its influence on vorticity will continue to pose challenges for both observationalists and modelers.

APPENDIX

Estimation of Errors in the Lagrangian Circulation Analysis Using Synthetic Dual-Doppler Wind Syntheses Derived from a Numerical Simulation of a Supercell

Errors in the calculation of the circulation about a material circuit are due to both errors in the locations of the parcels comprising the circuit, as well as errors in the winds interpolated to the circuit. The contribution to circulation errors from random errors in the wind velocity components is relatively insignificant. For example, for a standard deviation of random u and v (w) errors of 1 m s^{-1} ($0.002z$ m s^{-1}, where z is in meters), which compares well with the wind velocity errors obtained in the Majcen et al. (2008) study (see their Table 2), the circulation errors for circuit A (Fig. 1b) are only 0.01–0.03×10^5 m^2 s^{-1} in the first 8 min of backward integration, and 0.03–0.04×10^5 m^2 s^{-1} in the last 8 min of backward integration. The circulation errors were estimated from 500 integrations of the trajectories of the parcels comprising the material circuits, with the three-dimensional wind syntheses used to compute the trajectories being randomly perturbed in each realization, such that the perturbations of the u, v, and w wind components had a Gaussian distribution, zero mean, and the aforementioned standard deviations. Even for a threefold increase in the magnitude of the random u, v, and w errors, circulation errors are still generally less than 10%. Moreover, circulation calculations are insensitive to pure bias errors, given that circulation involves an integral about a closed circuit.

The actual errors in three-dimensional wind retrievals, however, are typically neither random nor pure bias errors (i.e., they have structure). Missing data regions can further complicate the distribution of errors. For example, radial velocities contaminated by ground clutter are removed prior to interpolating the raw data to a grid, but the regions of missing data can adversely affect the gridded radial velocity fields and ultimately the synthesized three-dimensional winds, especially at low
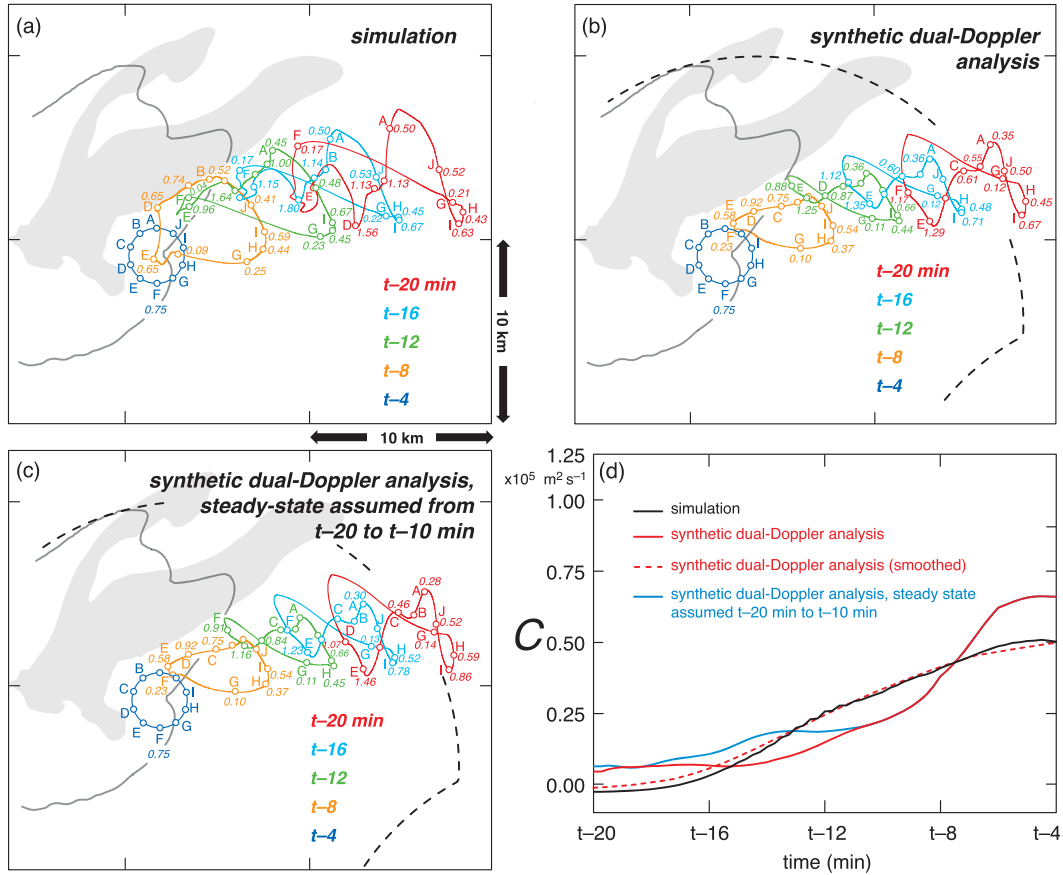
FIG. A1. Horizontal projections of a material circuit integrated backward in time from $t = 36$ min to $t = 20$ min (4 min and 20 min, respectively, before the development of a strong cyclonic vortex at the surface) using (a) the three-dimensional wind fields of the numerical simulation, (b) synthetic dual-Doppler wind fields derived from the simulation, and (c) synthetic dual-Doppler wind fields, but assuming a steady state in the last 10 min of the backward integration, as was assumed in the calculations in section 4. The material circuit comprises 10 000 parcels and is a 1.5-km-radius ring centered on the location of maximum vertical vorticity at $z = 0.75$ km at $t = 36$ min. The horizontal projection of the circuit is shown every 4 min. Every 1000th parcel is indicated with a marker, and select markers are labeled with the letters A–J and altitudes in km. Gray shading indicates rainwater at $z = 0.75$ km in excess of 1 g kg^{-1}. The $\theta'_\rho = -0.5$ K contour at $z = 0.125$ km is drawn as a dark gray line (this can be considered a proxy for the gust front position). The synthetic dual-Doppler lobe (for a 30° minimum interbeam angle) is indicated in (b) and (c) with the dashed black line. (d) The circulation C time series are shown (see legend). A smoothed time series of C also is shown for the synthetic analysis in which no steady-state assumption was made. The smoothing was accomplished using a triangular filter having a half-radius of 3 min.

levels. In the Goshen County storm in particular, there was extensive editing of the raw radial velocities owing to ground-clutter contamination in the inflow and along the southern fringe of the forward-flank radar echo (Fig. 3c; also see Figs. 3d–f of Part I). Furthermore, there may well be *unedited* radial velocities that have been biased by part of the radar beam having intercepted ground targets.

The credibility of the circulation calculations of section 4 was evaluated by retrieving the three-dimensional wind field from synthetic dual-Doppler "scanning" of a numerically simulated supercell, and comparing the circulation evolution diagnosed from the retrieved wind

fields to the evolution of circulation diagnosed from the simulated wind fields. The methodology and numerical simulation are identical to those used by Majcen et al. (2008). The simulation has a horizontal and vertical grid spacing of 250 m and was initialized with the sounding observed in the environment of the Del City, Oklahoma, supercell [see Majcen et al. (2008) for the details of the model configuration]. A cyclonically rotating, rightward-propagating supercell develops quickly in the simulation owing to the long, curved (the vertical shear vector veers with height) hodograph of the environmental wind profile. A well-defined hook "echo" is evident at low levels in the simulated rainwater field (Fig. A1a) by

$t = 40$ min. A strong cyclonic vortex also is present at this time; the vortex has a vertical vorticity of 0.066 s^{-1} at the surface.

A pair of synthetic radar volumes were obtained in a way that mimics the data collection during the pretornadic phase of the Goshen County storm (refer to Part I). The volumes were produced every 2 min and comprised 12 elevation angles ranging from $0.5°$ to $16.0°$. The beamwidth is infinitesimally narrow; model wind fields were interpolated to the synthetic radar beams every 100 m in range and $1°$ in azimuth. The two radars were positioned approximately 20 km east-southeast and southeast of the supercell, respectively (cf. Fig. A1b herein and Fig. 4 of Part I). The length of the baseline (15 km) matched that of DOW6 and DOW7, as did the orientation of the baseline. Random errors having a standard deviation of 1 m s^{-1} were added to the radial velocities derived from the simulated wind fields to introduce noise. No attempt was made to emulate radial velocity contamination by ground clutter. Three-dimensional wind fields were retrieved in nearly the exact same way that the observed wind fields were retrieved (i.e., identical grid spacing, objective analysis parameters, wind synthesis technique, etc.). One minor difference between the actual and synthetic data collection is that the simulated storm was approximately stationary relative to the radars. Moreover, volumes were collected instantaneously. Thus, there are no errors in the synthetic dual-Doppler-derived wind fields from storm motion and/or evolution.

A material circuit was tracked backward from $t = 36$ min (4 min prior to the development of the strong surface vortex) to $t = 20$ min using (i) the three-dimensional wind fields (the fields were saved every 30 s) of the numerical simulation (Fig. A1a), (ii) the synthetic dual-Doppler-derived wind fields (Fig. A1b), and (iii) the synthetic dual-Doppler wind fields, but assuming a steady state in the last 10 min of backward integration (Fig. A1c), as was assumed in the calculations of section 4. The material circuit comprises 10 000 parcels and is a 1.5–km-radius ring centered on the location of maximum vertical vorticity at $z = 0.75$ km at $t = 36$ min ($\zeta_{max} = 0.031$ s^{-1}); i.e., the approach follows that of section 4. In the retrieved wind fields, the horizontal winds below the data horizon at $z = 0.25$ km are set to the horizontal winds at $z = 0.25$ km (w is linearly interpolated between $z = 0.25$ km and the surface, where it vanishes), consistent with the free-slip lower boundary condition of the simulation.

Although the trajectories derived from the simulation output and retrieved wind fields are qualitatively similar (Figs. A1a–c), even when a steady state is assumed for 10 min, errors in the circulation tendency about the material circuit diagnosed from the retrieved wind field (Fig. A1d) are, not surprisingly, considerably larger than the practically negligible errors attributable to purely random wind component errors (the trajectories and circulation diagnosed from the simulation are regarded as the truth). The circulation errors are largely attributable to small-scale differences in the geometries of the circuits, particularly the vertical projections. The rmse of the values of C diagnosed from the retrieved wind fields during the 16-min backward integration of the circuit's trajectories (Fig. A1d) is 0.08×10^5 m^2 s^{-1}, and DC/Dt implied by the same time series is at times much larger than the DC/Dt diagnosed from the simulation wind fields (e.g., near $t = 28$ min, or 8 min prior to the development of the strong surface vortex). Note that the largest error in C is at the start of the backward integration. This is indeed surprising and demonstrates that C errors are introduced by the objective analysis and three-dimensional wind synthesis even when trajectory errors are absent. In this particular instance, it appears that the large C error at the initial time is due to the presence of a strong vortex and large velocity gradients by that time. The large velocity gradients were not well represented in the objectively analyzed radial velocity fields and ensuing three-dimensional wind synthesis.

In summary, the quantitative details of the time series of circulation about the material circuits are probably not trustworthy in general, especially on short time scales (less than $\sim$3–4 min). It is no doubt safer to infer longer-term trends (note the dashed trace in Fig. A1d). Using the trajectories to identify source regions of air parcels (e.g., whether they originate in the warm sector or in the outflow) appears to be well justified. The 10-min steady-state assumption is not a significant error source, at least not for the case simulated. Lastly, the statements above are made with the following caveat: there could be additional errors attributable to (edited or unedited) raw radial velocities that have been contaminated by ground clutter and adversely affect the objective analyses and wind syntheses. Such errors are nearly impossible to quantify and potentially could affect even the long-term diagnosed circulation trends.

REFERENCES

Adlerman, E. J., K. K. Droegemeier, and R. P. Davies-Jones, 1999: A numerical simulation of cyclic mesocyclogenesis. *J. Atmos. Sci.,* **56,** 2045–2069.

Byko, Z., P. Markowski, Y. Richardson, J. Wurman, and E. Adlerman, 2009: Descending reflectivity cores in supercell thunderstorms observed by mobile radars and in a high-resolution numerical simulation. *Wea. Forecasting,* **24,** 155–186.

Craven, J. P., and H. E. Brooks, 2004: Baseline climatology of sounding derived parameters associated with deep, moist convection. *Natl. Wea. Dig.,* **28,** 13–24.

Dahl, J. M. L., M. D. Parker, and L. J. Wicker, 2011: On the development of large surface vorticity in high-resolution supercell simulations. Preprints, *14th Conf. on Mesoscale Processes,* Los Angeles, CA, Amer. Meteor. Soc., 7.4. [Available online at https://ams.confex.com/ams/14Meso15ARAM/webprogram/Paper191179.html.]

Davies-Jones, R. P., 1982a: A new look at the vorticity equation with application to tornadogenesis. Preprints, *12th Conf. on Severe Local Storms,* San Antonio, TX, Amer. Meteor. Soc., 249–252.

——, 1982b: Observational and theoretical aspects of tornadogenesis. *Intense Atmospheric Vortices.* L. Bengtsson and J. Lighthill, Eds., Springer-Verlag, 175–189.

——, 1984: Streamwise vorticity: The origin of updraft rotation in supercell storms. *J. Atmos. Sci.,* **41,** 2991–3006.

——, 2000: A Lagrangian model for baroclinic genesis of mesoscale vortices. Part I: Theory. *J. Atmos. Sci.,* **57,** 715–736.

——, 2008: Can a descending rain curtain in a supercell instigate tornadogenesis barotropically? *J. Atmos. Sci.,* **65,** 2469–2497.

——, and H. E. Brooks, 1993: Mesocyclogenesis from a theoretical perspective. *The Tornado: Its Structure, Dynamics, Prediction, and Hazards, Geophys. Monogr.,* Vol. 79, Amer. Geophys. Union, 105–114.

——, R. J. Trapp, and H. B. Bluestein, 2001: Tornadoes and tornadic storms. *Severe Convective Storms, Meteor. Monogr.,* No. 50, Amer. Meteor. Soc., 167–221.

Doswell, C. A., III, and D. W. Burgess, 1993: Tornadoes and tornadic storms: A review of conceptual models. *The Tornado: Its Structure, Dynamics, Prediction, and Hazards, Geophys. Monogr.,* Vol. 79, Amer. Geophys. Union, 161–172.

——, and J. S. Evans, 2003: Proximity sounding analysis for derechos and supercells: An assessment of similarities and differences. *Atmos. Res.,* **67–68,** 117–133.

Dowell, D. C., and H. B. Bluestein, 1997: The Arcadia, Oklahoma, storm of 17 May 1981: Analysis of a supercell during tornadogenesis. *Mon. Wea. Rev.,* **125,** 2562–2582.

Gal-Chen, T., 1978: A method for the initialization of the anelastic equations: Implications for matching models with observations. *Mon. Wea. Rev.,* **106,** 587–606.

Grzych, M. L., B. D. Lee, and C. A. Finley, 2007: Thermodynamic analysis of supercell rear-flank downdrafts from Project ANSWERS. *Mon. Wea. Rev.,* **135,** 240–246.

Hane, C. E., and P. S. Ray, 1985: Pressure and buoyancy fields derived from Doppler radar data in a tornadic thunderstorm. *J. Atmos. Sci.,* **42,** 18–35.

Hirth, B. D., J. L. Schroeder, and C. C. Weiss, 2008: Surface analysis of the rear-flank downdraft outflow in two tornadic supercells. *Mon. Wea. Rev.,* **136,** 2344–2363.

Kennedy, A. D., E. N. Rasmussen, and J. M. Straka, 2007a: A visual observation of the 6 June 2005 descending reflectivity core. *Electron. J. Severe Storms Meteor.,* **2** (6).

——, J. M. Straka, and E. N. Rasmussen, 2007b: A statistical study of the association of DRCs with supercells and tornadoes. *Wea. Forecasting,* **22,** 1192–1199.

Kis, A. K., J. M. Straka, and K. M. Kanak, 2008: On the role of descending rain curtains in tornadogenesis. Preprints, *24th Conf. on Severe Local Storms,* Savannah, GA, Amer. Meteor. Soc., 14.1. [Available online at https://ams.confex.com/ams/24SLS/techprogram/paper_142115.htm.]

Klemp, J. B., and R. Rotunno, 1983: A study of the tornadic region within a supercell thunderstorm. *J. Atmos. Sci.,* **40,** 359–377.

Lemon, L. R., and C. A. Doswell III, 1979: Severe thunderstorm evolution and mesocyclone structure as related to tornadogenesis. *Mon. Wea. Rev.,* **107,** 1184–1197.

Lewellen, D. C., and W. S. Lewellen, 2007: Near-surface intensification of tornado vortices. *J. Atmos. Sci.,* **64,** 2176–2194.

Lewellen, W. S., D. C. Lewellen, and R. I. Sykes, 1997: Large-eddy simulation of a tornado's interaction with the surface. *J. Atmos. Sci.,* **54,** 581–605.

Lilly, D. K., 1982: The development and maintenance of rotation in convective storms. *Intense Atmospheric Vortices,* L. Bengtsson and J. Lighthill, Eds., Springer-Verlag, 149–160.

Majcen, M., P. Markowski, Y. Richardson, D. Dowell, and J. Wurman, 2008: Multipass objective analyses of radar data. *J. Atmos. Oceanic Technol.,* **25,** 1845–1858.

Markowski, P. M., J. M. Straka, and E. N. Rasmussen, 2002: Direct surface thermodynamic observations within the rear-flank downdrafts of nontornadic and tornadic supercells. *Mon. Wea. Rev.,* **130,** 1692–1721.

——, C. Hannon, J. Frame, E. Lancaster, A. Pietrycha, R. Edwards, and R. Thompson, 2003: Characteristics of vertical wind profiles near supercells obtained from the Rapid Update Cycle. *Wea. Forecasting,* **18,** 1262–1272.

——, E. N. Rasmussen, J. M. Straka, R. P. Davies-Jones, Y. Richardson, and J. Trapp, 2008: Vortex lines within low-level mesocyclones obtained from pseudo-dual-Doppler radar observations. *Mon. Wea. Rev.,* **136,** 3513–3535.

——, M. Majcen, and Y. P. Richardson, 2010: Near-surface vortexgenesis in idealized three-dimensional numerical simulations involving a heat source and a heat sink in a vertically sheared environment. Preprints, *25th Conf. on Severe Local Storms,* Denver, CO, Amer. Meteor. Soc., 15.1. [Available online at http://ams.confex.com/ams/25SLS/techprogram/paper_176112.htm.]

——, ——, ——, J. Marquis, and J. Wurman, 2011: Characteristics of the wind field in three nontornadic low-level mesocyclones observed by the Doppler on Wheels radars. *Electron. J. Severe Storms Meteor.,* **6** (3).

——, and Coauthors, 2012: The pretornadic phase of the Goshen County, Wyoming, supercell of 5 June 2009 intercepted by VORTEX2. Part I: Evolution of kinematic and surface thermodynamic fields. *Mon. Wea. Rev.,* **140,** 2887–2915.

Marquis, J., Y. Richardson, P. Markowski, D. Dowell, and J. Wurman, 2012: Tornado maintenance investigated with high-resolution dual-Doppler and EnKF analysis. *Mon. Wea. Rev.,* **140,** 3–27.

Mashiko, W., H. Niino, and T. Kato, 2009: Numerical simulation of tornadogenesis in an outer-rainband minisupercell of Typhoon Shanshan on 17 September 2006. *Mon. Wea. Rev.,* **137,** 4238–4260.

Nowotarski, C. J., P. M. Markowski, and Y. P. Richardson, 2011: The characteristics of numerically simulated supercell storms situated over statically stable boundary layers. *Mon. Wea. Rev.,* **139,** 3139–3162.

Rasmussen, E. N., 2003: Refined supercell and tornado forecast parameters. *Wea. Forecasting,* **18,** 530–535.

——, J. M. Straka, M. S. Gilmore, and R. Davies-Jones, 2006: A preliminary survey of rear-flank descending reflectivity cores in supercell storms. *Wea. Forecasting,* **21,** 923–938.

Ray, P. S., C. L. Ziegler, W. Bumgarner, and R. J. Serafin, 1980: Single- and multiple-Doppler radar observations of tornadic storms. *Mon. Wea. Rev.,* **108,** 1607–1625.

Rotunno, R., 1981: On the evolution of thunderstorm rotation. *Mon. Wea. Rev.,* **109,** 577–586.

——, and J. B. Klemp, 1985: On the rotation and propagation of simulated supercell thunderstorms. *J. Atmos. Sci.,* **42,** 271–292.

Shabbott, C. J., and P. M. Markowski, 2006: Surface in situ observations within the outflow of forward-flank downdrafts of supercell thunderstorms. *Mon. Wea. Rev.,* **134,** 1422–1441.

Straka, J. M., E. N. Rasmussen, R. P. Davies-Jones, and P. M. Markowski, 2007: An observational and idealized numerical examination of low-level counter-rotating vortices toward the rear flank of supercells. *Electron. J. Severe Storms Meteor.,* **2** (8).

Thompson, R. L., R. Edwards, J. A. Hart, K. L. Elmore, and P. M. Markowski, 2003: Close proximity soundings within supercell environments obtained from the Rapid Update Cycle. *Wea. Forecasting,* **18,** 1243–1261.

Trapp, R. J., and B. H. Fiedler, 1995: Tornado-like vortexgenesis in a simplified numerical model. *J. Atmos. Sci.,* **52,** 3757–3778.

——, G. J. Stumpf, and K. L. Manross, 2005: A reassessment of the percentage of tornadic mesocyclones. *Wea. Forecasting,* **20,** 680–687.

Wakimoto, R. M., H. Cai, and H. V. Murphey, 2004: The Superior, Nebraska, supercell during BAMEX. *Bull. Amer. Meteor. Soc.,* **85,** 1095–1106.

Walko, R. L., 1993: Tornado spin-up beneath a convective cell: Required basic structure of the near-field boundary layer winds. *The Tornado: Its Structure, Dynamics, Prediction, and Hazards, Geophys. Monogr.,* Vol. 79, Amer. Geophys. Union, 89–95.

Wicker, L. J., 1996: The role of near surface wind shear on low-level mesocyclone generation and tornadoes. Preprints, *18th Conf. on Severe Local Storms,* San Francisco, CA, Amer. Meteor. Soc., 115–119.

Wurman, J., D. Dowell, Y. Richardson, P. Markowski, E. Rasmussen, D. Burgess, L. Wicker, and H. Bluestein, 2012: The Second Verification of the Origins of Rotation in Tornadoes Experiment: VORTEX2. *Bull. Amer. Meteor. Soc.,* **93,** 1147–1170.